

# A two-scale hydromagnetic dynamo experiment

By U. MÜLLER<sup>1</sup>, R. STIEGLITZ<sup>1</sup> AND S. HORANYI<sup>2</sup>

<sup>1</sup>Forschungszentrum Karlsruhe, Institut für Kern- und Energietechnik, Hermann-von-Helmholtz-Platz 1,  
76344 Eggenstein-Leopoldshafen, Germany

<sup>2</sup>KFKI Atomic Energy Research Institute, Budapest, Hungary

(Received 10 January 2003 and in revised form 5 August 2003)

The Karlsruhe Dynamo experiment is aimed at showing that an array of columnar helical vortices in liquid sodium, confined in a cylindrical container, can generate a magnetic field by self-excitation. In three test series it has been demonstrated that magnetic self-excitation occurs and a permanent magnetic saturation field develops which oscillates about a well-defined mean value for fixed flow rates. Dynamo action is observed as an imperfect bifurcation from a seed magnetic field of the environment. Two quasi-dipolar magnetic fields of opposite direction have been realized. A transition between these two states can be enforced through imposition of a sufficiently strong external magnetic perturbation on the existent dynamo field. These perturbations were induced with the aid of two Helmholtz coils. A time series analysis of the magnetic field fluctuations shows several characteristic dynamic features, which are in agreement with theoretical predictions from turbulence models available in the literature.

---

## 1. Introduction

Systems capable of converting mechanical into electromagnetic energy are called dynamos. Technical dynamos are commonly utilized for electricity generation. In principle these power generators are constructed in a complex way using multiply connected copper wiring arranged in several coils combined with ferromagnetic material, which rotate relatively to each other in such a way that self-excitation of an electro-dynamic state occurs. A detailed description of a technical dynamo can be found in any textbook of fundamental and applied physics. These technical dynamos are different from homogeneous dynamos, which in principle originate from vortical flows in electrically conducting homogeneous fluids contained in singly connected domains where the fluid flow may be driven by external or internal forces. The existence of such homogeneous hydromagnetic dynamos is not obvious, as any induced current in the homogeneous conductor may short-circuit and vanish from the conductor without amplifying a seed magnetic field, which together with the fluid motion generates the current.

The investigation of homogeneous dynamos has received much attention in geo- and astrophysics during the last fifty years, as it is generally accepted today that the origin of planetary, solar and even galactic magnetic fields is dynamo action in the interior of these celestial bodies or ‘clouds’. The historical development and the present state of the art can be obtained from numerous survey articles on this subject (see e.g. Busse 1978, 2000; Rittinghouse Inglis 1981; Rädler 1995; Moss 1997; Fearn 1998; Glatzmaier & Roberts 2000; Gailitis *et al.* 2002). The vast majority of the research has been focused on the theory of homogeneous dynamos. Only recently have

a number of experimental research programs been initiated to demonstrate homogeneous dynamo action in the laboratory. So far only in two laboratories, at the Physics Institute in Riga and at the Forschungszentrum Karlsruhe, have dynamo actions been successfully realized in an experiment (see Gailitis *et al.* 2001; Stieglitz & Müller 2001).

In this article we report the results of hydrodynamic dynamo experiments performed at the Forschungszentrum Karlsruhe. The article is organized as follows. Section 2 outlines the theoretical background of the dynamo experiment. Section 3 describes the experimental set-up and the measuring techniques. The experimental results are presented in §4. Finally, in §5 experimental and theoretical results are compared and discussed. In §6 some conclusions and perspectives are given.

## 2. The theoretical background

### 2.1. General aspects

It is generally accepted today that planetary dynamos are driven by buoyant convection in the liquid and electrically conducting core of celestial bodies. A general description of the dynamo process requires the solution of the complete set of coupled thermo-fluid-dynamic and electro-magnetic transport equations in finite, e.g. spherical, domains together with appropriate boundary conditions. This is a formidable mathematical problem, which only recently has been tackled with some success by several research groups utilizing advanced methods of computational fluid dynamics (CFD). The state of the art of the numerical approach to the convection-driven geodynamo problem has been described recently by Jones (2000), Busse (2000), Glatzmaier & Roberts (2000) and Glatzmaier (2002).

In the past the thermo-fluiddynamic and the magneto-hydrodynamic aspects of the planetary dynamo problem have often been considered separately in order to reduce the complexity of the overall problem to mathematically treatable or experimentally accessible subtasks. Thus, the thermal and solutal convection problem in rotating spheres and the kinetic dynamo problem of vortex flows have been treated in parallel.

From numerous theoretical and experimental investigations on buoyant convection in rapidly rotating spheres or spherical shells a convincing picture of the coherent flow structures in the liquid core of rotating planets has emerged (see Busse 1971, 1992, 1994; Busse & Carrigan 1974, 1976; Carrigan & Busse 1983; Zhang 1992; Sumita & Olson 1999; Aubert *et al.* 2001). A characteristic feature of the internal, buoyancy-driven flow in major planets is an assembly of large columnar vortices with axes parallel to the planet's axis of rotation. These vortices are of the Taylor–Proudman type in the near-equator range and of the Bénard type in the pole regions.

The associated hydromagnetic dynamo problem starts from the assumption that the velocity field is known or can be directly calculated from a given pressure or conservative force distribution. This reduced problem has recently been reformulated by Tilgner & Busse (2002). It is governed by the following set of dimensionless equations for the velocity  $\mathbf{v}$  the pressure  $p$  and the magnetic induction  $\mathbf{B}$ :

$$\partial_t \mathbf{v} + (\mathbf{v} \cdot \nabla) \mathbf{v} = -\nabla p + \frac{1}{Re} \nabla^2 \mathbf{v} + (\nabla \times \mathbf{B}) \times \mathbf{B} + \mathbf{f}, \quad (2.1)$$

$$\mathbf{v} \cdot \nabla = 0, \quad (2.2)$$

$$\partial_t \mathbf{B} + \nabla \times (\mathbf{B} \cdot \nabla) = \frac{1}{Rm} \nabla^2 \mathbf{B}, \quad (2.3)$$

$$\mathbf{v} \cdot \mathbf{B} = 0. \quad (2.4)$$

Here the hydrodynamic and magnetic Reynolds numbers are defined as

$$Re = \frac{U_0 d}{\nu}, \quad Rm = \frac{U_0 d}{\lambda}, \quad (2.5)$$

where  $U_0$  is a reference velocity,  $d$  a characteristic dimension of the velocity and magnetic field and  $\nu$  and  $\lambda$  are the viscous and the magnetic diffusivities. The reference velocity  $U_0$  may be defined by the volumetric flow rate  $\dot{V}$  in the laboratory model and a particular flow cross-section, characterized by its hydraulic diameter. Aside from the pressure  $p$ , a forcing function  $f$  has been introduced in order to simulate specific velocity distributions of laboratory dynamos. It is noticed here that the relative influence of viscous and Joule dissipation in equations (2.1) and (2.3) is governed by the ratio of the two Reynolds numbers  $Rm/Re$ , which is commonly termed the magnetic Prandtl number  $Pm = \nu/\lambda$ . For any numerical treatment of the system (2.1) particular difficulties arise if  $Pm \ll 1$ , as e.g. in case of sodium flows.

## 2.2. Onset of dynamo action

If the onset of dynamo action is of primary interest, the model equations (2.1)–(2.4) can be simplified further by considering specific velocity distributions as given. The velocity may be introduced into equation (2.3). Together with boundary conditions for the magnetic field at the surface of the flow domain, equations (2.3) and (2.4) define the so-called kinematic dynamo problem. A solution of this problem can be obtained in the form of a complex product function

$$\mathbf{B}(x, t) = \exp(\gamma t) \cdot \mathbf{b}(x), \quad (2.6)$$

where the growth rate is determined by the associated boundary eigenvalue problem. For  $R(\gamma) > 0$  self-excitation of the magnetic field, i.e. dynamo action, occurs; for  $R(\gamma) < 0$  any initially given seed magnetic field decays in time. Naturally, the growth rate depends on the magnetic Reynolds number  $Rm$  and the structure of the velocity field.

With regard to an anticipated quasi-regular vortex flow structure in the liquid core of a planet it is of particular interest to investigate the potential for dynamo action caused by periodic velocity fields. Roberts (1970, 1972) did this for infinitely extended fields. He proved mathematically that dynamos exist “for almost all steady spatially periodic motions of a homogeneous conducting fluid at almost all values of the conductivity”. Childress (1967) derived an existence proof for magnetic self-excitation in a spherical liquid conductor containing a quasi-periodic velocity distribution. The proof is constructive and is based on the presumption of scale separation between the period length  $L$  and the radius of the sphere  $R$ . Gailitis (1967) elaborated an analytical solution of this problem using the Mean Field Theory of Steenbeck, Krause & Rädler (1966). He showed that in liquid sodium and for geometrical dimensions of 1 m for the sphere and 0.1 m for the velocity period the velocity should be of the order of  $|\mathbf{v}| \approx 1 \text{ m s}^{-1}$  to achieve self-excitation. Furthermore, he concluded from the current distribution that a cylindrical confinement of the periodic velocity field would be more favourable for dynamo action at low velocities, i.e. at low magnetic Reynolds numbers. Busse (1992) derived an approximate solution for the kinematic dynamo problem for a periodic velocity field in a cylindrical confinement. He started from a Roberts-type velocity distribution, as sketched in figure 1(a), and placed it in a cylinder, as shown in figure 1(b). In his analysis he assumed that the period length  $L = 2a$  is much smaller than the cylinder radius  $r_0$  and its height  $D$  and that the only boundary condition at the cylinder surface  $S$  is a vanishing normal component

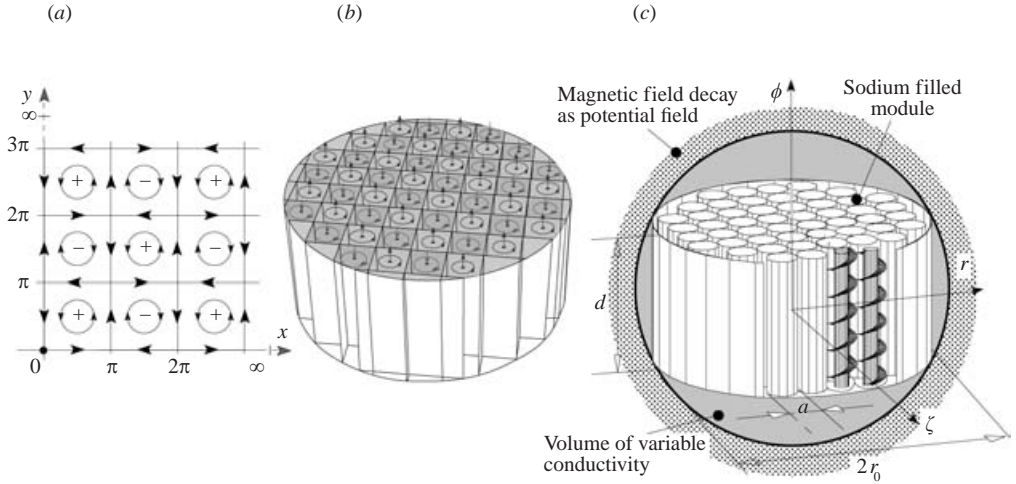


FIGURE 1. (a) Non-confined periodic vortex pattern after Roberts (1972) and in modified form after Busse (1992); (b) Busse’s vortex arrangement confined in a cylindrical domain; (c) Tilgner’s (1997) and the Rädler *et al.* (1998) vortex arrangement in a sphere.

of the mean electric current density  $\mathbf{j}$ . The scale separation together with mean field methods enabled him to derive a criterion for the onset of dynamo action in analytical form.

Based on his calculations Busse (1992) suggested demonstrating the feasibility of this two-scale homogeneous dynamo in the laboratory and designing an experiment with liquid sodium as the test fluid according to his model conception (cf. figure 1b). With regard to the coherent and quasi-periodic columnar vortex structures there is some similarity between the conjectured flow pattern in the liquid core of fast rotating planets and the suggested laboratory model.

Tilgner (1997, 2002) and Rädler *et al.* (1998, 2002a) improved Busse’s original model decisively with regard to conditions in the laboratory. They embedded the cylinder containing the vortices into a sphere bounded by an insulating environment outside and filled with stagnant conducting fluid in the spherical sections (see figure 1c). They solved equations (2.3) and (2.4) with appropriate boundary and matching conditions for the current density and the magnetic field. Using different numerical approaches (spectral methods, mean field theory) both obtained basically the same results: the non-symmetric mode with an azimuthally order number  $m=1$  shows the largest amplification for all combinations of volumetric flow rates, i.e. magnetic Reynolds numbers. The mean magnetic field has a ‘spiral staircase’ structure in the near field and a dipolar orientation perpendicular to the cylinder axis in the far distance.

### 2.3. Saturated dynamo states

An interesting aspect of the hydrodynamic dynamo beyond the marginal state (which we shall denote as the ‘critical’ state) is the mechanism which leads to a saturated magnetic state. The saturation effect is principally caused by the feedback of the Lorentz forces  $\mathbf{f}_L = \mathbf{j} \times \mathbf{B}$  on the velocity field described by equation (2.1). For liquid metals like sodium and mercury, commonly used in the laboratory, the kinematic viscosity  $\nu$  is much smaller than the magnetic diffusivity  $\lambda$  (i.e.  $\nu_{\text{sodium}} = 0.6 \times 10^{-6} \text{ m}^2 \text{ s}^{-1}$ ,  $\lambda_{\text{sodium}} = 0.1 \text{ m}^2 \text{ s}^{-1}$ ). This implies that the hydrodynamic Reynolds number  $Re$  is much larger than the magnetic Reynolds number  $Rm$ . For supercritical conditions

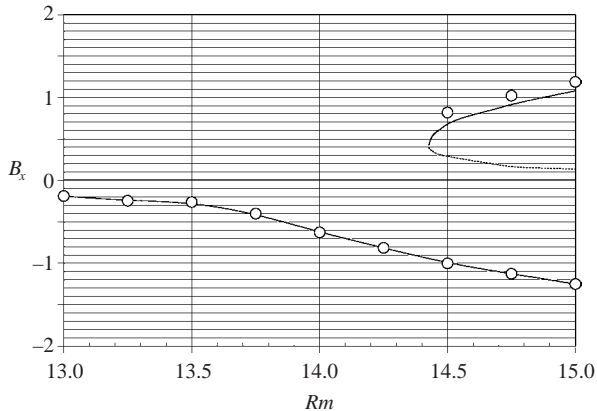


FIGURE 2. The bifurcation diagram for the Karlsruhe Dynamo experiment calculated by Tilgner & Busse (2002) for the dimensionless component  $B_x$  and equal volumetric flow rates;  $\circ$ , numerical results; —, fit to the low-mode approximation formula (2.7) for steady conditions. (For more details see the cited literature.)

with  $Rm > 1$  we have  $Re \sim O(10^5 - 10^6)$ . This means that the flow is fully turbulent. Compared to turbulent shear stresses the viscous shear stresses and thus the viscous term in equation (2.1)  $(1/Re)(\nabla^2 v)$  can be neglected. Nevertheless, using Reynolds representation for turbulent flow the form of equation (2.1) may be maintained for fully turbulent flow conditions, if the velocity is defined as a mean value and the Reynolds number is based on an assumed constant eddy viscosity  $\nu_t$  (see, e.g., Hinze 1975). Tilgner & Busse (2002) studied this modified problem numerically, employing spectral methods for the spatial resolution and finite differences for the time integration. They found that the saturated stationary dynamo states bifurcate imperfectly from a hydrodynamic state, which is effected with an environmental seed magnetic field.

Figure 2 shows a typical bifurcation graph obtained by Tilgner & Busse (2002) for a parameter set compatible with the Karlsruhe Dynamo experiment. The graph shows the continuous and the isolated branches of supercritical dynamo states characterized by opposite field directions (for more details on bifurcation theory see Golubitzky & Schaeffer 1985).

Tilgner & Busse (2002) have also derived a model equation in a low-order amplitude approximation for  $\mathbf{B}$ . Their results are based on the general form of equations (2.1)–(2.4) and suggest that the magnetic field saturates with increasing field intensity. They obtain an evolution equation for  $\mathbf{B}$  in the form

$$\frac{d\mathbf{B}}{dt} = \left[ \left( \frac{Rm}{Rm_c} - 1 \right) - \frac{\beta}{Rm_c} |\mathbf{B}|^2 \right] \mathbf{B} + \mathbf{B}_0, \quad (2.7)$$

where  $\mathbf{B}_0$  accounts for the driving effect of an external seed field and  $Rm_c$  is the value for the marginal state in case of a vanishing seed field. The stationary supercritical states are recovered for  $d\mathbf{B}/dt = 0$  as the solution of a cubic algebraic equation for  $\mathbf{B}$ .

Equation (2.7) contains three independent coefficients,  $Rm_{crit}$ ,  $\mathbf{B}_0$  and  $\beta$ , which may be adjusted to either numerical or experimental data.  $Rm_{crit}$  may be taken from calculations for the ideal kinematic state without a seed field.  $\mathbf{B}_0$  and  $\beta$  can be determined by fitting the third-order equation to numerically or experimentally obtained

solutions on the continuous branch. Then, the model equation predicts the discontinuous branch in the same approximation and the quality of the approximation may be tested by comparison with corresponding numerical and experimental results.

Also, Rädler *et al.* (2002b) have studied the nonlinear behaviour of dynamo action in the Karlsruhe test facility by employing generalized mean field methods. Some of their results will be compared with our experimental findings in § 5.

#### 2.4. Some comments on MHD turbulence

In a sodium experiment dynamo action may occur for magnetic Reynolds numbers  $Rm = \bar{u}d_h/\lambda > 1$  and at high hydrodynamic Reynolds numbers  $Re = \bar{u}d_h/\nu$  of  $O(10^6)$  due to the greatly different values of the magnetic and viscous diffusivities ( $d_h$  is the relevant hydraulic diameter of a helical vortex, see figure 1, and the velocity  $\bar{u}$  is the volumetric flux in it). Thus, the channel flow is fully turbulent and all magnetohydrodynamic variables in equations (2.1)–(2.4) are affected by turbulent fluctuations and may be decomposed into a mean and a fluctuating part as

$$\mathbf{v} = \bar{\mathbf{v}} + \mathbf{v}', \quad p = \bar{p} + p', \quad \mathbf{B} = \bar{\mathbf{B}} + \mathbf{B}'. \quad (2.8)$$

The quality of these turbulent fluctuations can be judged by utilizing the characteristic functions of random data analysis. In processing our measured time signals we evaluated the mean values, the probability density functions (PDF) and the higher moments, the variance, skewness and flatness ( $\sigma^2, S, K$ ). The temporal and spatial coherence of the signals can be obtained from their auto- and cross-correlation functions (ACF, CCF) as well as from their Fourier spectra, i.e. the power spectral density (PSD).

For a more subtle analysis of turbulent processes the exchange and transport of energy between structures of different size for velocity and magnetic field must be considered, where the structures can be imagined as eddies of either the velocity or current field. The scale of these structures is bounded by viscous and Joule dissipation on the lower side, i.e. by the Kolmogorov (1941) time and length scales (see Hinze 1975). For the viscous and Joule dissipation they are

$$\tau_{Kv} = \left(\frac{\nu}{\varepsilon}\right)^{1/2}, \quad L_{Kv} = \left(\frac{\nu^3}{\varepsilon}\right)^{1/4}; \quad \tau_{K\lambda} = \left(\frac{\lambda}{\varepsilon}\right)^{1/2}, \quad L_{K\lambda} = \left(\frac{\lambda^3}{\varepsilon}\right)^{1/4}. \quad (2.9)$$

Here  $\varepsilon$  is the specific energy flux, which is dissipated. It may be defined for channel flow by the pressure loss  $\Delta p$ , the volumetric flow rate  $\dot{V}$ , and the fluid mass  $M$  as

$$\varepsilon = \dot{V} \Delta p / M. \quad (2.10)$$

It is obvious that in turbulent sodium flow  $L_{Kv} \ll L_{K\lambda}$ . Therefore, the Joule dissipation time and length scales are particularly relevant for turbulent sodium flow. The ratio of each of these quantities is directly related to the magnetic Prandtl number defined as  $Pm = \nu/\lambda$ .

The dimensions of the test facility determine the upper limit of scales  $L$ , in our case typically the velocity  $\bar{u}$  is determined by the diameter  $d_h$  of a vortex generator, and the magnetic field and the associated currents are determined by the diameter of the cylindrical test module  $2r_0$  and its height  $D$ .

The energy transfer between the different scales is commonly discussed in turbulence theory by a spectral decomposition of the state variables and a spectral transformation of the governing equations, in our case equations (2.1)–(2.4). The variables in the form of power spectral density functions (PSD) depend on wavenumbers  $k_n$  and frequencies  $\omega_n$  which are related to the corresponding spectral length and time scales

of the turbulent structures as

$$k_n = \frac{2\pi}{L_n}, \quad \omega_n = \frac{2\pi}{\tau_n}. \quad (2.11)$$

For turbulent channel flow, where  $u^*/\bar{u} \ll 1$  holds ( $u^*$  denotes the standard deviation), Taylor's hypothesis (see Hinze 1975) applies and  $k_n$  can be expressed by  $\omega_n$  and the mean velocity as  $k_n = \omega_n/\bar{u}$  or  $k_n = 2\pi f_n/\bar{u}$ .

Here we recall briefly some relevant relationships from the literature for turbulent magnetohydrodynamic (MHD) flows, which we shall use later on. The spectral distribution of the turbulent energies is commonly obtained by a Fourier transformation of the auto-correlation function of the velocity and magnetic field fluctuations respectively. The turbulent kinetic and magnetic energies  $E^V$  and  $E^M$  are thus replaced by their spectral distribution functions  $E_k^V$  and  $E_k^M$ .†

In three-dimensional turbulent flow, not influenced, or at most very weakly influenced by magnetic fields, the kinetic energy of large-scale motion is transferred to smaller-scale motions in a cascade of successive flow instabilities induced by vortex stretching and shearing processes. This occurs without dissipative losses in a wavenumber range between the low wavenumber  $k_L$  of the large-scale inertial flow and the high wavenumber  $k_{Kv}$  for viscous dissipative small-scale flow. Based on the assumption that the flux of kinetic energy is conserved, Kolmogorov (1941) derived a relation between the spectral energy density  $E_k^V$ , the injected energy rate  $\varepsilon$  and the wavenumber  $k$  in the form

$$E_k^V = c_K \varepsilon^{2/3} k^{-5/3} \quad \text{for } k_L < k < k_{Kv},$$

with  $c_K$  a dimensionless constant and  $k_{Kv}$  the wavenumber based on the Kolmogorov viscous dissipative length scale (cf. Hinze 1975). This is known as the inertial range of kinetic energy transfer by a nonlinear interaction of vortices and for negligible viscous dissipation. For weak intensities a large-scale magnetic field behaves like a passive vector in a turbulent velocity field. It can be shown by a spectral transformation of equation (2.3) that the fluctuations of the magnetic field obey the same spectral law as the velocity, i.e.

$$E_k^V \sim E_k^M \sim k^{-5/3}. \quad (2.12)$$

This spectral behaviour has been observed in experiments in a fairly wide range of magnetic field intensities and for different turbulent flow conditions such as turbulent flow behind grids (Kolesnikov & Tsinober 1974; Alemany *et al.* 1979) and in turbulent swirling flows in spherical containers (Peffley, Cawthorne & Lathrop 2000). It has also been corroborated by direct numerical model calculations of Biscamp & Mueller (2000) and Brandenburg (2001).

The transfer process has to be modified in conducting fluids in the presence of a magnetic field if Lorentz forces, originating from the large-scale magnetic field and the small-scale electric currents initiated by the velocity fluctuations, significantly influence the small-scale motions. This may be an external magnetic field or a self-excited mean magnetic field  $\bar{B}$ . The energy transfer occurs through locally interacting Alfvén waves in an inertial range of wavenumbers, which is limited from above by the Joule dissipative wavenumber  $k_{K\lambda} = 2\pi(\varepsilon/\lambda^3)^{1/4}$ . Iroshnikov (1963) and Kraichnan (1965) derived an interdependence between the spectral energy  $E_k^V$ , the dissipation  $\varepsilon$  and the Alfvén velocity  $V_a = \bar{B}/\sqrt{\mu\rho}$  where  $\mu$  is the magnetic permeability. They

† The formalism of spectral decomposition holds strictly only for homogeneous turbulent flows in infinite domains (see textbooks on turbulent flows, e.g. Hinze 1975).

used dimensional arguments based on the assumption that the energy flux achieves equilibrium and an equipartition of kinetic and magnetic energy exists in the range considered. They arrive at the following power relationship for the kinetic spectral energy:

$$E_k^V(k) = c_K(\varepsilon V_a)^{1/2} k^{-3/2} \quad \text{for } k_L < k < k_{K\lambda}. \quad (2.13)$$

This relationship holds as long as the velocity and magnetic field fluctuations are spatially uncorrelated, which is true for mean magnetic fields of moderate intensities and for an interaction of Alfvénic waves with the same size wavenumbers. However, if the velocity and magnetic field become correlated at increasing magnetic field intensities, the energy exchange by Alfvén wave interaction may occur in a wider range of wave numbers. Equipartition between kinetic and magnetic energy can no longer be anticipated. Grappin, Pouquet & Leorat (1983) have treated this case, which is outlined in some detail in Biskamp's (1993) textbook.† Using Elsasser variables  $\mathbf{Z}^\pm = \mathbf{v} \pm \mathbf{B}/(\rho\mu)^{1/2}$  they consider modified spectral quantities based on these variables and relate them to the energy spectral densities  $E_k^V(k)$  and  $E_k^M(k)$ . By definition the following relations hold between the total spectral energy  $E_k$  and the Elsasser spectral energy quantities  $E_k^\pm$ :

$$E_k = E_k^V + E_k^M = E_k^+ + E_k^-.$$

Making assumptions of strong separation of scales in the inertial range, but requiring equal dissipation wavenumbers  $k_{K\lambda}$  for both Elsasser spectral energy densities, Grappin *et al.* (1983) derived the power law

$$E_K^\pm = C_1 \lambda V_a \left( \frac{k}{k_{K\lambda}} \right)^{-m_\pm} \quad (2.14)$$

for the inertial range with  $m_+ + m_- = 3$ .

This correlation merges into the Iroshnikov–Kraichnan (1963, 1965) relationship under the assumption of equipartition between kinetic and magnetic spectral energies. Otherwise, in the case of a strong correlation between the velocity and magnetic field and for non-equipartition of energies one of the power coefficients  $m_+$  or  $m_-$  vanishes while the other approaches the value 3. That is  $E_K^\pm \sim k^{-3}$ . It can be shown (cf. Biskamp 1993) that in general in the inertial range  $E_k^M - E_k^V > 0$  holds, and thus one obtains for the power spectral density

$$E_k^M \sim k^{-3}$$

(for more details see Biskamp 1993 and Grappin *et al.* 1983). So far this kind of inertial spectral behaviour has not been validated by experimental observations.

If large-scale magnetic fields have an intensity such that Lorentz forces become significant for the momentum transfer, even local homogeneity of the velocity field cannot be sustained. Velocity fluctuations in the direction of the magnetic field and perpendicular to it are dampened differently by Joule dissipation and there is a quasi-equilibrium transfer of energy between the fluctuations of different spatial orientation. The effect has been analysed in detail by Alemany *et al.* (1979). The effect should be

† It should be noticed here that Grappin *et al.* (1983) restricted their numerical investigations to the case of equal momentum and magnetic diffusivities:  $v = \lambda$ , i.e. for a magnetic Prandtl number  $Pm = v/\lambda = 1$ . In our investigations with liquid sodium the magnetic Prandtl number is of the order  $10^{-5}$ . Thus, the magnetic diffusivity dominates. Nevertheless, the general relationships of Grappin *et al.* (1983) for the inertial spectral domain, as outlined by Biskamp (1993), hold also in our case, if  $\lambda$  is taken as the governing diffusivity and the associated Kolmogorov dissipation wavenumber  $k_{K\lambda}$  is used as the relevant reciprocal length scale.



observed if the interaction parameter  $N$  based on the local quantities of the velocity field, the vortex dimension  $\ell$  and the magnetic field intensity  $B_0$ , is of the order 1, i.e.  $N = (\sigma B_0^2 \ell) / (\rho u) \approx O(1)$ .

With regard to our model velocity field in figure 1 and dynamo action,  $B_0$  would correspond to the self-excited magnetic field intensity  $|\mathbf{B}|$  and  $u$  to the mean helical velocity  $\bar{u}$  defined as the helical volumetric flux;  $\ell$  would correspond to the half-period  $\alpha$  of the velocity field. An equivalent interpretation of  $N \approx 1$  is that the transport time of energy or the vortex turnover time  $\tau_t \sim \ell/u^*$  is of the same order as the Joule dissipation time scale  $\tau_j \sim \rho/(\sigma B_0^2)$ .

With  $\ell \sim 1/k$  and a spectral representation of the velocity,  $u \sim (E_k^V k)^{1/2}$ , this results in the power relationship:

$$E_K^V \sim \tau_j^{-2} k^{-3}. \quad (2.15)$$

This spectral relationship has been confirmed in an inertial–dissipative range by extensive experimental investigations of Alemany *et al.* (1979) and recently by Messadek & Moreau (2002).

The spectral MHD energy under the influence of Joule dissipation, but still in the inertial range of fluid dynamics, has been analysed by Moffatt (1961). Assuming that  $1 \ll Rm \ll Re$  holds, he finds that the magnetic spectral energy distribution is correlated to the kinetic spectral energy as

$$E_k^M \approx \lambda^{-2} k^{-2} E_K^V. \quad (2.16)$$

Furthermore, using for the kinetic spectral energy  $E_K^V$  the Kolmogorov relationship (2.12) for a weak interaction between the magnetic and the velocity field, he derives the following expression for the magnetic spectral energy in the Joule dissipative regime of wavenumbers  $k_{K\lambda} < k < k_{Kv}$ :

$$E_k^M = \frac{9}{4} Rm \bar{B}_o^2 \varepsilon^{2/3} \lambda^{-2} k^{-11/3} \quad \text{for } k_{K\lambda} < k < k_{Kv}. \quad (2.17)$$

Here  $\bar{B}_o^2$  is a measure of the magnetic energy of the large-scale magnetic field, e.g. an external magnetic field or, with a similar effect, a self-excited dynamo field. If one proceeds with the same reasoning, but applies the relationship (2.15) of Alemany *et al.* (1979) for the velocity power spectrum, then one obtains the relation

$$E_k^M \propto k^{-5} \quad (2.18)$$

in the dissipative range. In this case, however, a strong correlation between the velocity field and the induced large-scale magnetic field should apply. The decay of the magnetic spectral density in the Joule dissipative range  $k > k_{K\lambda}$  according to Moffatt's relationship (2.17) has been corroborated by measurements of Odier, Pinton & Fauve (1998) and Marie *et al.* (2001). Peffley *et al.* (2000) report evidence for an even stronger decay such as  $E_K^M \sim k^{-4.5}$ .

So far we have considered the spectral energy transport from large-scale vortices and eddy currents downward to smaller scales. It has been found, however, from model calculations that in three-dimensional turbulent vortex flow small-scale magnetic fluctuations associated with small-scale eddy currents may build up large-scale magnetic fields by self-organization. This effect is known as the reverse cascade of spectral energy transfer and is closely related to the conservation of magnetic helicity  $H^M$ . This process has been described theoretically for helical turbulence in a series of papers by Frisch *et al.* (1975), Pouquet, Frisch & Leorat (1976) and Leorat, Pouquet & Frisch (1981). Here we outline some results of Pouquet *et al.*, which we consider to be relevant for our observations.

The magnetic helicity is a conserved quantity, if dissipative effects are neglected (cf. Biskamp 1993). Frisch *et al.* (1975) pointed out that in the spectral domain of helical, isotropic MHD turbulence a self-organization of magnetic helicity towards larger scales may occur, if this quantity is permanently injected into the system at a fixed rate and a characteristic wavenumber  $k_{in}$ . Pouquet *et al.* (1976) corroborated this reverse cascade by extensive numerical calculations using closure approximations for turbulent helical flow in the spectral domain. They chose a magnetic Prandtl number  $Pm = 1$ . They found that together with the reverse helicity cascade a reverse energy cascade exists. In the spectral domain their results indicate a quasi-stationary behaviour in form of power relationships

$$H_k^M(k) \sim k^{-2}, \quad E_k^M(k) \sim k^{-1}, \quad (2.19)$$

for the magnetic spectral helicity  $H_k^M$  and the magnetic spectral energy  $E_k^M$ . They substantiated these findings by dimensional arguments of the Kolmogorov type for the reverse inertial transport mechanisms. They argue that there should exist a unique functional dependence between the relevant quantities  $E_k^M$  and  $H_k^M$  on the one hand and the effective helicity injection rate  $\varepsilon_{eff}^M$  and the wavenumber  $k$  on the other hand. The effective helicity injection rate may differ from the total injection rate, as part of it may cascade downward into helicities of smaller scale and finally dissipate. A similar statement holds for the injected energy. The dimensional considerations result in the relationships

$$E_k^M(k) = C_1(\varepsilon_{eff}^M)^{2/3}k^{-1}, \quad H_k^M(k) = C_2(\varepsilon_{eff}^M)^{2/3}k^{-2} \quad \text{for } k < k_{in}, \quad (2.20)$$

where  $C_1$  and  $C_2$  are dimensionless constants. Furthermore, it has been shown that under equilibrium conditions (cf. Pouquet *et al.* 1976) the spectral component of the magnetic helicity is related to the kinematic helicity as  $H_k^M \propto k^{-2}H_k^V$ . Equivalently

$$\varepsilon_k^M \propto k^{-2}\varepsilon_k^V \quad (2.21)$$

holds. Here  $H_k^V$  is the spectral representation of the kinetic helicity (cf. Biskamp 1993). From an experimental point of view the injected kinetic helicity and its specific scale  $k_{in}^{-1}$  is the control parameter for dynamo action rather than the magnetic helicity.

A result similar to the outcome from closure model calculations of Pouquet *et al.* (1976) has been reported by Brandenburg (2001). He applies direct numerical spectral methods and finds spectral energy propagation into the range of smaller wavelength  $k$ , if helicity is injected into the system at an intermediate wavenumber. However, instead of a continuous power distribution with a behaviour proportional to  $\sim k^{-1}$  he found only an envelope for the helicity waves which follows approximately a  $\sim k^{-1}$  power law.†

Following Pouquet *et al.* (1976) again, we cite an estimation for the time  $T$  it takes to build up a large-scale magnetic field of dimension  $L \sim k_L^{-1}$  from a small-scale turbulent seed field characterized by an injection length scale  $\ell_{in} \sim k_{in}^{-1}$ . It is reasonable to define this time to be proportional to the ratio

$$T \sim \left( \frac{H^M}{\varepsilon_{eff}^M} \right). \quad (2.22)$$

Pouquet *et al.* obtained (cf. the original literature)

$$T \sim (\varepsilon_{eff}^M)^{-1/3} L.$$

† The frequency and wavelength spectra are equivalent, if Taylor's Hypothesis holds.

Using relationship (2.21) results in

$$T \sim C_2 (\varepsilon_{\text{eff}}^V \rho_{\text{in}}^2)^{-1/3} L. \quad (2.23)$$

We shall refer to these relationships outlined for turbulent MHD flow in our discussions of the experimental results in §§4.1 and 5.

### 3. The dynamo test facility and instrumentation

The Karlsruhe dynamo test facility has been described in detail by Stieglitz & Müller (1996). Here we restrict ourselves to a brief outline of the main features. The test rig consists essentially of a cylindrical dynamo module which contains 52 vortex generators connected to three different loops each of which is equipped with an MHD feed pump of about 210 kW power and a heat exchanger to ensure constant temperature in the liquid sodium during the experimental runs. Using water–steam heat exchangers provides a constant operation temperature within a threshold of  $\pm 1^\circ\text{K}$  during runs of several hours.

The module and the loop are fabricated entirely of stainless steel. The shroud of the vortex generators as well as the inner tube consist of 1 mm thick stainless steel sheets or tubing material, whereas the guide vanes generating the vortex flow are fabricated from 0.5 mm thick sheet metal. Taking into account the different temperature-dependent specific electric conductivities of stainless steel and sodium in both the axial and radial directions separately the effective magnetic diffusivity is increased by 8.5–9% compared to that of pure sodium. Thus, operating the dynamo module in a temperature range between  $120^\circ\text{C} < T < 125^\circ\text{C}$  yields a magnetic diffusivity of  $\lambda = 0.1 \text{ m}^2 \text{ s}^{-1}$  with an accuracy of  $\pm 0.002 \text{ m}^2 \text{ s}^{-1}$ . In order to ensure optimal electrical contact between the liquid sodium and the stainless steel channel walls, the wetting of the wall material was achieved by operating the sodium loops at elevated temperatures of  $350^\circ\text{C}$ – $400^\circ\text{C}$  for more than 24 hours.

A technical sketch of the dynamo module, the individual vortex generator and the operational set up is given in figure 3. A reference coordinate system is also indicated. The ideal helical flow of the vortex pattern in figure 1(a) is approximated by a quasi-vortex-free flow in the central duct and a spiral flow in the annular gap enforced by a helical baffle plate. The diameter of a vortex generator is  $a = 0.21 \text{ m}$ ; the inner duct diameter is  $a_i = 0.1 \text{ m}$ . The height of a complete helical winding is  $h = 0.19 \text{ m}$ . The radius of the cylindrical container is  $r_0 = 0.93 \text{ m}$ , its height is  $D = 0.98 \text{ m}$ . The vortex generators are connected at their ends by bends for the central flow and by fitting channels for the helical flow. The helical flow in the vortex generators is provided by two separate loops each supplying 26 helical flow channels arranged in a right and left semi-section of the cylinder.

The central flow is controlled by a third sodium loop. The maximum capacity of the MHD pumps is  $\dot{V} = 150 \text{ m}^3 \text{ h}^{-1}$  each. The pressure drop across the module in each of the three independent channel systems is measured by sensitive capacitance pressure gauges from KULITE Int. with an accuracy of  $\delta p = \pm 5 \times 10^2 \text{ Pa}$ . The frequency resolution of the pressure gauges is about 400 Hz. The sodium volumetric flow rate in each of the three loops is determined by electromagnetic (EM) flow meters which are calibrated via a gyrostatic absolute mass flow meter before each measurement campaign to give errors less than  $(\delta \dot{V})/\dot{V} < 0.3\%$ .

The module is located in a separate room and sheltered from electromagnetic stray fields from the MHD pumps and EM flow meters by a floor of soft iron plates. Thus, the intensity of the stray field in the test room is less than 0.5 G, i.e.

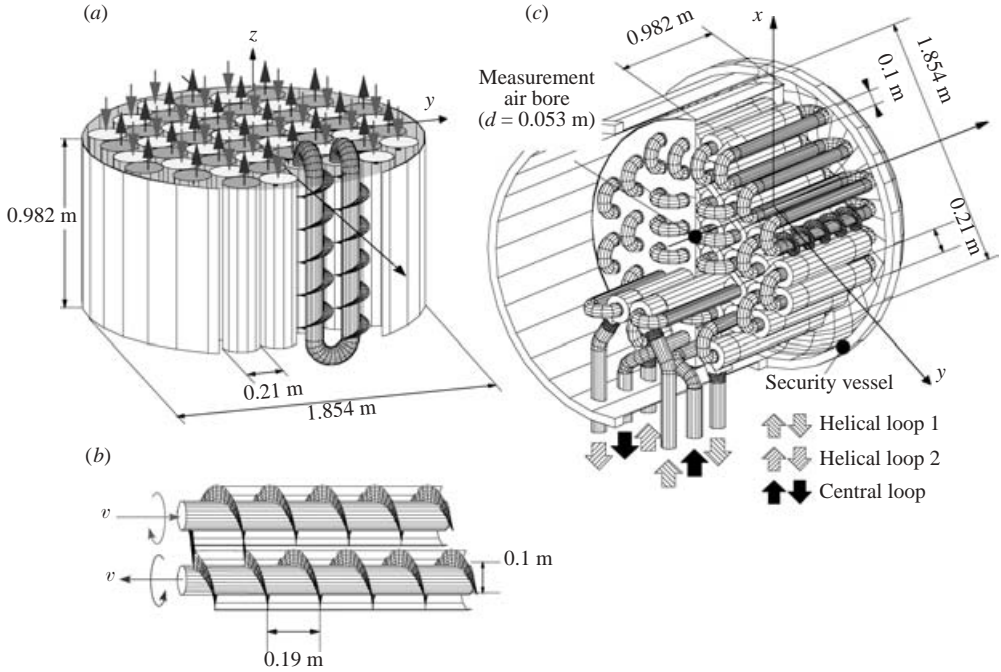


FIGURE 3. Semi-technical sketch of the Karlsruhe dynamo test module: (a) internal structure and velocity distribution, (b) vortex generator, (c) technical design with a reference coordinate system.

of the order of the Earth's magnetic field. The magnetic field in the test module is measured by Hall sensors from Bell Inc. Because of the strict temperature control a resolution of  $\delta B/B \leq 0.03\%$  for the highest field intensities could be ensured at a frequency resolution of 300 Hz. The data recording of each signal acquisition (pressures, temperatures, flow rates, Hall signals) was performed at a frequency of 512 Hz using fast 16-bit acquisition cards of the Keithley Company.

During the dynamo tests the magnetic field was recorded at two fixed locations near the 'equator' of the cylinder, separated by  $120^\circ$ , and at variable positions along the cylinder axis between the centre and the 'north pole' using a traversable probe. The Hall probe can be moved in the  $z$ -direction in a stainless steel tube of 0.05 m in diameter, which penetrates the module along its axis. Using the induction equation (2.3) and the properties for stainless steel a conservative estimate gives that the effective probe diameter affects its frequency wide-band ratio only in a frequency range  $f > 300$  Hz. Two Hall sensors ( $H3$ ,  $H4$ ) are fixed to the traversable probe. One ( $H3$ ) is capable of measuring all three components ( $B_x$ ,  $B_y$ ,  $B_z$ ) of the  $B$ -field, the other ( $H4$ ) located a distance of 135 mm from  $H3$  measures  $B_y$  only. The Hall sensors near the equator ( $H5$ ,  $H6$ ) are arranged to measure the radial component of the field.  $H5$  also measures the axial component  $B_z$ . The sensor locations are schematically shown in figure 4.

Before each measurement campaign the pressure transducers, the EM flow meters and the Hall sensors were calibrated to ensure high measuring accuracy and to avoid systematic errors. In particular the flow rate was calibrated before each coherent set of measurements. Also the environmental seed magnetic field was repeatedly recorded with the traversable Hall sensors for vanishing volumetric flow rates and at

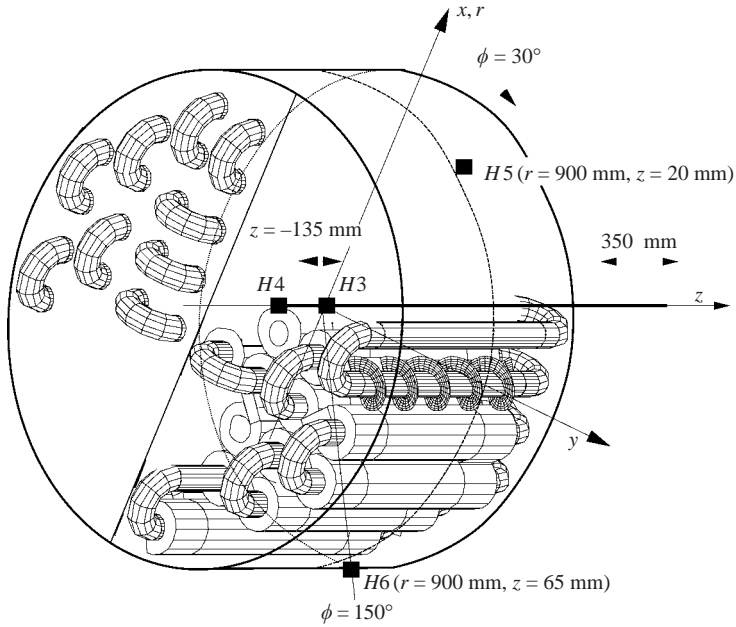


FIGURE 4. Sketch of the locations of the Hall sensors in the test module; location  $H3$ : two Hall sensors to measure three field components  $B_x, B_y, B_z$ ; location  $H4$ : one Hall sensor to measure  $B_y$ ; location  $H5$ : one Hall sensor to measure two components  $B_z$  and  $B_r$ , i.e. the radial component; location  $H6$ : one Hall sensor to measure the radial component  $B_r$ .

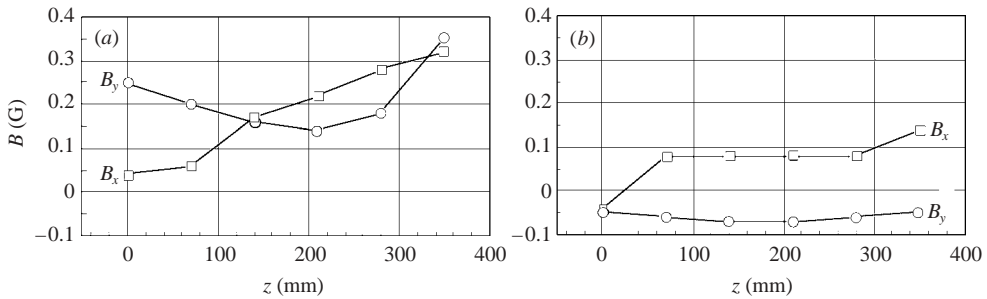


FIGURE 5. The distribution of the seed magnetic field along the module axis in the range  $0 \leq z \leq 350$  mm recorded at (a) the beginning and (b) the end of a measuring campaign. There is a noticeable change in the local characteristic of the seed field. Volumetric flow rates  $\dot{V}_C = \dot{V}_{1,2} = 0$ .

intermediate subcritical flow rates. Two typical recordings for the mean magnetic field intensities on the module axis in the range  $0 \leq z \leq 350$  mm are shown in figure 5(a, b) for zero flow rates. The graphs show that the seed magnetic field is subject to variations during a measuring period. However, the observed variations were always smaller than the local intensity of the Earth’s magnetic field.

Furthermore, arrays of mobile compass needles were attached to two vertical wood boards, one placed sideways and one in front of the cylindrical dynamo vessel, in order to obtain a qualitative impression of the structure of the generated magnetic field. From the orientation of the compass needles during dynamo action the global structure of the magnetic field could be identified. In support of this qualitative

instrumentation the normal component of the magnetic field with regard to the vertical boards was measured using a carry-on Hall probe in some cases.

The test module was generally operated in two modes. In order to study the onset of self-excitation and the saturation of the magnetic field at supercritical conditions, the volumetric flow rates in the three loops were scanned up (or down) for flow rate variations  $0.1 \leq \delta V \leq 5 \text{ m}^3 \text{ h}^{-1}$  within time intervals of typically between 1 and 10 min. The time intervals between the variations ensured that a new hydromagnetic equilibrium, i.e. a saturated dynamo state, was achieved. One flow rate was varied, while the other helical or central flow rates were kept constant, or all flow rates were simultaneously varied at the same rate.

The other operation mode of the test facility is for long-term runs at constant volumetric flow rates. Time series of signals of the magnetic field components, pressure differences and volumetric flow rates were recorded during time intervals of 1200 up to 4000 s.

## 4. Results

### 4.1. Self-excitation of the magnetic field

In our experiments we used time series signals recorded by Hall probes, EM flow meters and pressure transducers as indicators of dynamo action. Typical time signal recordings for the volumetric flow rates in the three loops, the three components of the magnetic field at the centre of the module (position *H3* in figure 4) and the pressure drop in the three channel systems of the module are shown in figure 6. In this experiment the two helical flow rates  $V_{H1}$  and  $V_{H2}$  were simultaneously raised stepwise from subcritical to supercritical conditions during a total period of 1600 s, while the central flow rate was kept constant at  $\dot{V}_C = 85$  or 86.

The signals for the first 1000 s are displayed. The magnetic field components follow the stepwise variation of the helical flow rates and achieve a saturation level during each time interval without flow rate variation. There is in particular no delay time between the rise time of the volumetric flow rate and that of the magnetic field components. An evaluation of the predicted self-organization time for the large-scale magnetic field according to relationship (2.23) of Pouquet *et al.* (1976) gives time scales of less than 0.6 s which are much smaller than any rise time realized for the pumping power, which is of the order of 50 s (see figure 6*b*). They are also considerably smaller than the overall magnetic diffusion time for the module, which is about 10 s. After a test run of 900 s the record shows a saturated  $B$ -field of  $|B| \sim 300 \text{ G}$  in the centre of the module, which has a strong  $x$ - and  $y$ -components and a small  $z$ -component.

In figure 7 the stationary states are plotted versus the helical flow rates. This graph shows a weak increase for lower, and a strong increase for higher, flow rates with a tendency to reduced growth rates at even higher flow rates. A point of inflection can be seen in the interpolation curve of the measured data points. The onset of dynamo action cannot be sharply allocated to a particular volumetric flow rate  $\dot{V}_H$ . The observation suggests a smooth rather than a sharp bifurcation, i.e. an imperfect bifurcation of the steady dynamo states from the hydrodynamic basic state. The onset of dynamo action may be defined by plotting the local magnetic energy, i.e.  $\overline{B^2}$  measured at position *H3*, versus flow rates. This is shown in figure 8(*a*). Self-excitation can be identified by the sudden linear increase of the magnetic energy. We use the intersection of the linear interpolation curve with the axis of flow rates as the marker for the beginning of self-excitation.

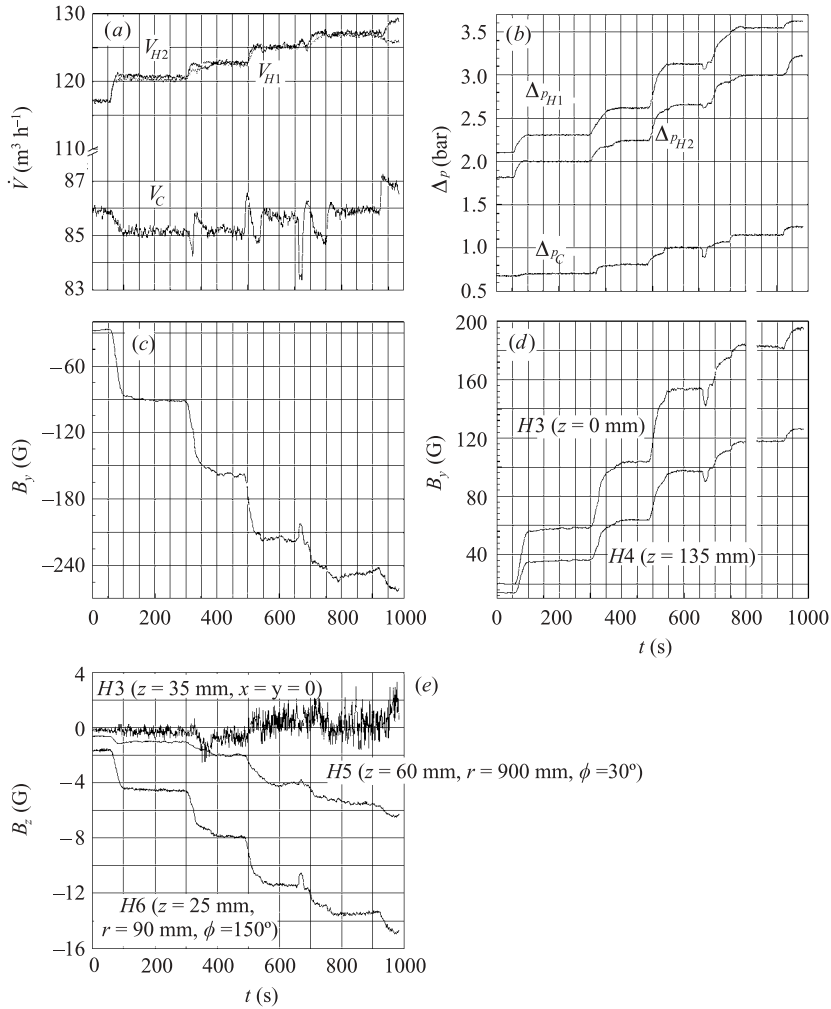


FIGURE 6. Time signal recordings for (a) volumetric flow rates; (b) pressure losses in the helical and central channels; (c–e) magnetic field components for an experimental operation with stepwise changing flow rates.

In a similar way as in the case of hydrodynamic bifurcation problems of shear flows, the pipe pressure loss across the module indicates the onset of self-excitation by a significant pressure increase due to the additional magnetohydrodynamic losses. In figure 8(b) the pressure differences between the inlet and outlet of the three loops at the test module are shown for the corresponding steady hydrodynamic and magnetohydrodynamic states.

The hydrodynamic and magnetohydrodynamic flow states can be distinguished by a change in the increment of the data sequence. The intersection of the linear interpolation curves for the hydrodynamic and the magnetohydrodynamic losses then defines experimentally to a good approximation the bifurcation point for this particular test run. Here, we emphasize that the pressure loss measurements in the three independent loops result in the same transition value within a margin of  $|\delta V_H| \leq 1 \text{ m}^3 \text{ h}^{-1}$ . Corresponding test runs were performed and evaluated for other fixed central and variable helical flow rates or in some cases vice versa.

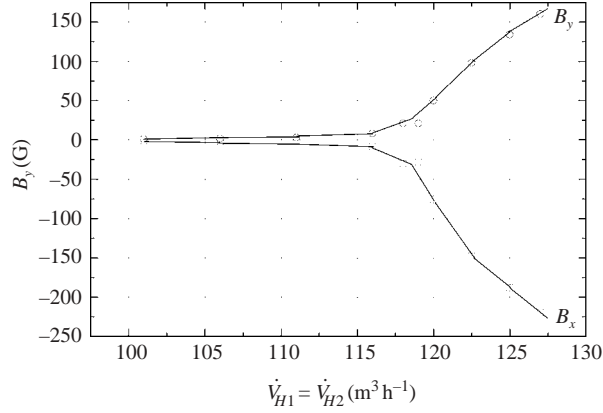


FIGURE 7. Magnetic field components  $B_x$  ( $\square$ ) and  $B_y$  ( $\circ$ ) for saturated steady dynamo states measured in the centre at  $H3$  for a constant central flow rate  $\dot{V}_C = 85 \text{ m}^3 \text{ h}^{-1}$  and variable helical flow rates  $110 < \dot{V}_{H1,2} < 130 \text{ m}^3 \text{ h}^{-1}$  – piecewise fit to the experimental data.

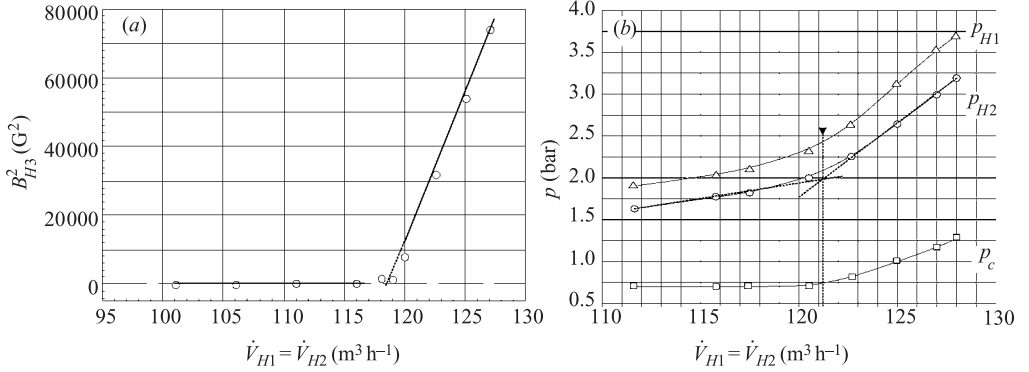


FIGURE 8. (a) Local magnetic energy in the centre at  $H3$  and (b) pressure losses in the helical and central piping systems of the test module under steady-state operation conditions for  $\dot{V}_C = 85 \text{ m}^3 \text{ h}^{-1}$ ,  $110 < \dot{V}_{H1,2} < 130 \text{ m}^3 \text{ h}^{-1}$  —, ---, fit to the data points.

The evaluation of the magnetic energy and the pressure losses results in a phase diagram of dynamo action for our test module. It is presented in a  $(\dot{V}_C/\dot{V}_H)$ - as well as in a  $(Rm_C, Rm_H)$ -plane. Hydrodynamic and dynamo states are separated by an interpolation line of hyperbolic character, which, within the error bounds of the instrumentation and the evaluation methods, represents both data sets within the error bounds of the instrumentation and the evaluation methods. This is seen in figure 9.

#### 4.2. The structure of the magnetic field

The overall structure of the dynamo fields at clearly supercritical conditions was examined by the orientation of an array of compass needles arranged on plane boards, which were placed vertically sideways and in front of the cylindrical test vessel. The needles can turn in the plane of the board and thus react to the magnetic field components in this plane. Moreover, using a carry-on Gauss meter the normal component of the field on the sideways-located board was measured. Figure 10 shows (a) the isoline graph of the normal component on the side-board and (b) the array of compass needles on the front board. This particular test was performed



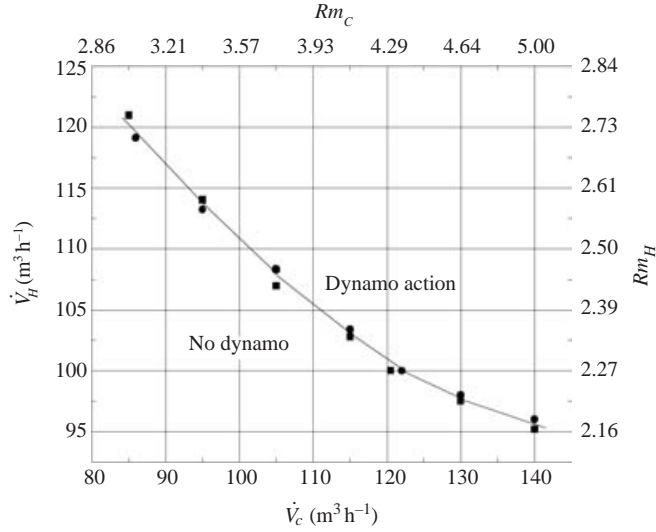


FIGURE 9. The state diagram for dynamo action for the Karlsruhe test module: ●, energy criterion; ■, pressure loss criterion; —, piecewise linear fit to experimental data. The magnetic Reynolds numbers  $Rm_C$  and  $Rm_H$  based on the hydraulic diameters of the central and helical channels respectively are defined in table 1 in the appendix.

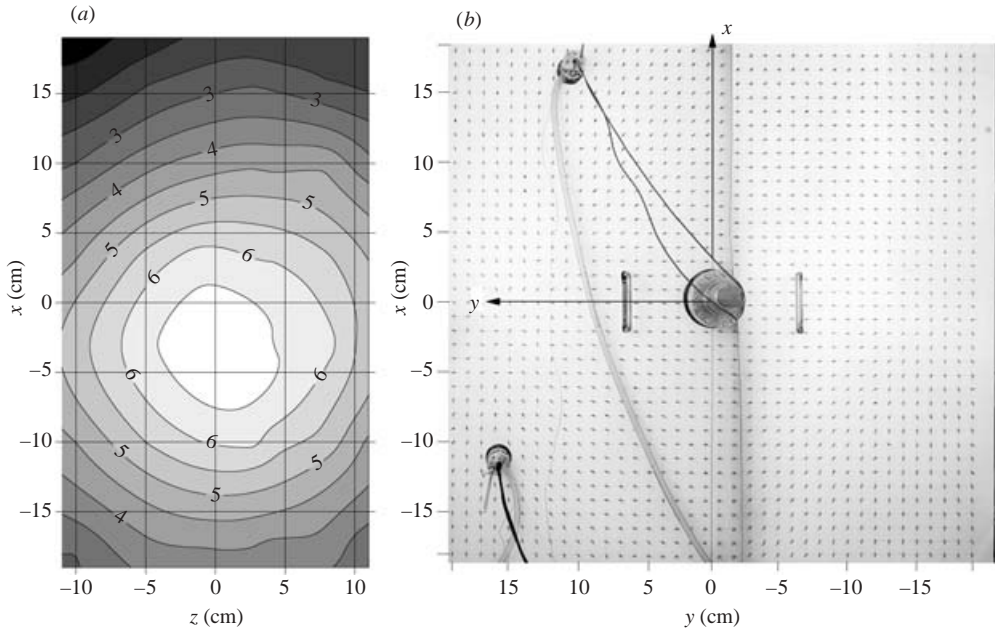


FIGURE 10. The global structure of the dynamo magnetic field: (a) isolines of  $B_y$ , i.e. the normal components of the magnetic field measured in the plane of the side-ways placed vertical board at position  $y = 1.67 \text{ m}$ ; the numbers in the isoline graph indicate the field intensity measured in Gauss; (b) array of compass needles arranged on a vertical board in front of the module and perpendicular to its axis at a position  $z = 1.04 \text{ m}$  from the centre. Experimental conditions:  $\dot{V}_C = 115 \text{ m}^3 \text{h}^{-1}$ ,  $\dot{V}_{H1,2} = 115 \text{ m}^3 \text{h}^{-1}$  and  $\lambda = 0.1 \text{ m}^3 \text{s}^{-1}$ .

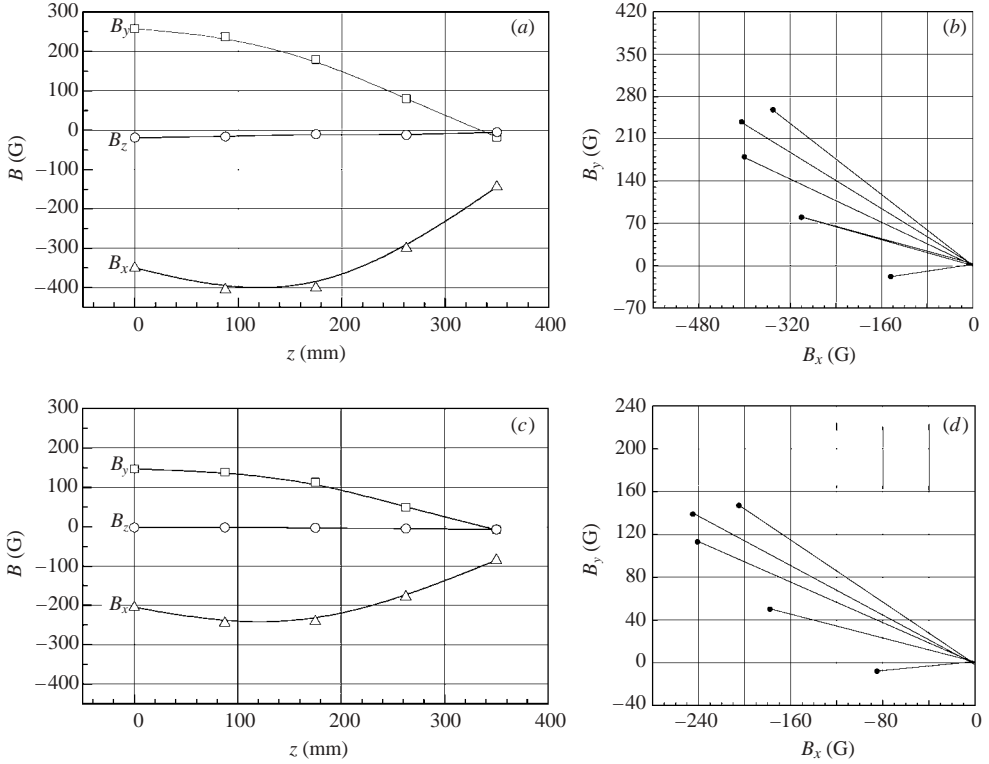


FIGURE 11. (a, c) Distribution of the intensities of the magnetic field components on the module axis in the range  $0 \leq z \leq 350$  mm for equal volumetric flow rates: (a)  $\dot{V}_H = \dot{V}_C = 115 \text{ m}^3 \text{ h}^{-1}$ ; (c)  $\dot{V}_H = \dot{V}_C = 110 \text{ m}^3 \text{ h}^{-1}$ . (b, d) Variation of the angle of inclination of the magnetic field relative to the module's position for (b)  $\dot{V}_H = \dot{V}_C = 115 \text{ m}^3 \text{ h}^{-1}$ ; (d)  $\dot{V}_H = \dot{V}_C = 110 \text{ m}^3 \text{ h}^{-1}$ .

for the volumetric flow rates  $\dot{V}_C = \dot{V}_{H1} = \dot{V}_{H2} = 115 \text{ m}^3 \text{ h}^{-1}$ . Figure 10(a) indicates a concentration of magnetic field lines near a centreline perpendicular to the cylinder axis of the module and suggests a dipole structure of the field. This impression is supported by the photo figure 10(b) showing the orientation of compass needles at the front side of the module. Two centres of random needle orientation are located at a certain distance from the two vertical rims of the plate and slightly below its horizontal centreline.

Between these centres and towards the plate periphery the needles show an orientation along lines of force, which are compatible with a quasi-dipole field whose axis passes through the module perpendicular to the cylinder axis. The level of the centre of largest field intensity of the isoline graph is compatible with the level of the areas of disorder in the needle array at the front board (see figure 10b).

Further insight into the local structure of the magnetic field is gained from the distribution of the field components along the cylinder axis obtained by traversing the Hall probe at location  $H3$  in the range  $0 \leq z \leq 350$  mm. This distribution is shown in figure 11(a) for the volumetric flow rate condition. There is only a small  $B_z$ -component compared to the  $B_x$  and  $B_y$  components. The maximum of the field intensity is not reached in the centre of the module. The maximum is, rather, slightly shifted toward a position  $z = 100$  mm. The angle of inclination  $\beta$  of the  $B$ -field vector to the  $x$ -coordinate axis changes in the range  $144^\circ \leq \beta \leq 188^\circ$  along the  $z$ -axis in the

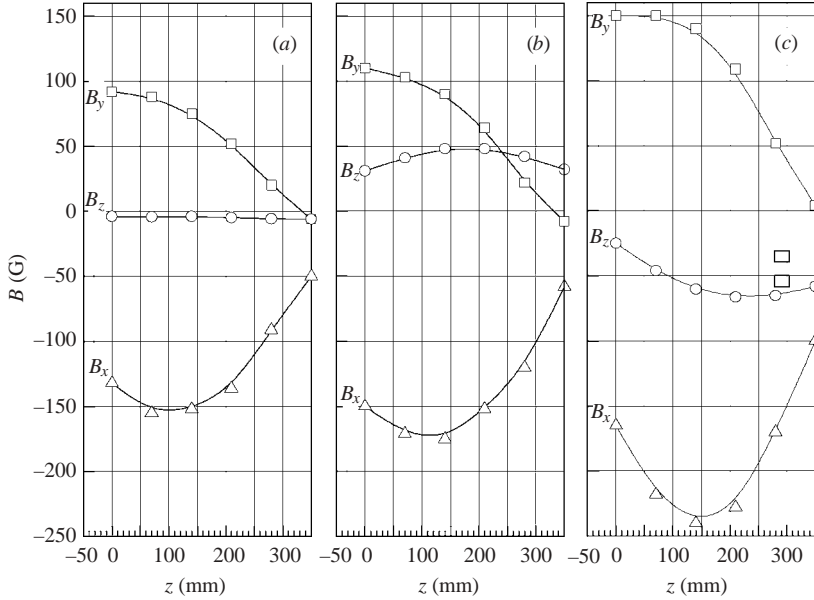


FIGURE 12. Distribution of the magnetic field components along the axis of the module in the range  $0 \leq z \leq 350$  mm for symmetric and non-symmetric flow distributions. (a)  $\dot{V}_{H1} = \dot{V}_{H2} = 100 \text{ m}^3 \text{ h}^{-1}$ ,  $\dot{V}_C = 128 \text{ m}^3 \text{ h}^{-1}$ ; (b)  $\dot{V}_{H1} = 85 \text{ m}^3 \text{ h}^{-1}$ ,  $\dot{V}_{H2} = 115 \text{ m}^3 \text{ h}^{-1}$ ,  $\dot{V}_C = 128 \text{ m}^3 \text{ h}^{-1}$ ; (c)  $\dot{V}_{H1} = 115 \text{ m}^3 \text{ h}^{-1}$ ,  $\dot{V}_{H2} = 85 \text{ m}^3 \text{ h}^{-1}$ ,  $\dot{V}_C = 128 \text{ m}^3 \text{ h}^{-1}$ .

range  $0 \leq z \leq 350$  mm. This is shown by the  $B$ -vector graph in figure 11(b). The  $B$ -field is twisted along the  $z$ -axis in the manner of a spiral staircase. At lower supercritical volumetric flow rates, e.g.  $\dot{V}_c = \dot{V}_{H1} = \dot{V}_{H2} = 110 \text{ m}^3 \text{ h}^{-1}$ , the general behaviour of the  $B$ -field on the  $z$ -axis is the same except that the intensities are reduced. The turning of the  $B$ -field vector along the  $z$ -axis is not significantly affected. This general observation is displayed in figures 11(c) and 11(d). Here the magnetic field vector turns about the  $z$ -axis by  $43^\circ$  from the inner to the outer measuring position. The intensity of the  $B$ -vector is noticeably reduced. In general, in the whole range of tested supercritical flow rates  $85 < \dot{V}_{H1} = \dot{V}_{H2} < 125 \text{ m}^3 \text{ h}^{-1}$  and  $85 < \dot{V}_c < 140 \text{ m}^3 \text{ h}^{-1}$  the measured turning angle of the magnetic field vector along the positive  $z$ -axis varied only modestly between  $40^\circ < \beta < 45^\circ$  along the positive  $z$ -axis.

The dynamo test facility can be operated with different flow rates in the three independent channel systems of the module. We investigated the influence of a non-symmetric velocity distribution on the structure of the dynamo magnetic field by feeding, e.g., one helical loop with a flow rate  $\dot{V}_{H1} = 85 \text{ m}^3 \text{ h}^{-1}$  and the second helical loop with  $\dot{V}_{H2} = 115 \text{ m}^3 \text{ h}^{-1}$  and vice versa at a constant flow rate of  $\dot{V}_c = 128 \text{ m}^3 \text{ h}^{-1}$  in the central loop. Figure 12 shows the measured distribution of the field components along the semi-axis of the module. Three situations are displayed by the graphs in figure 12: the distribution (a) for equal helical flow rates  $\dot{V}_{H1} = \dot{V}_{H2} = 100 \text{ m}^3 \text{ h}^{-1}$ , (b) for non-equal helical flow rates  $\dot{V}_{H1} = 85 \text{ m}^3 \text{ h}^{-1}$ ,  $\dot{V}_{H2} = 115 \text{ m}^3 \text{ h}^{-1}$  and (c) for the complementary case  $\dot{V}_{H1} = 115 \text{ m}^3 \text{ h}^{-1}$ ,  $\dot{V}_{H2} = 85 \text{ m}^3 \text{ h}^{-1}$ . The striking difference compared to the flow situation with equal helical flow rates is the greatly enhanced  $z$ -components of the magnetic field shown in figure 12(b, c). Depending on the shift of the helical flow rates from the reference case, positive or negative field components  $\bar{B}_z$  occurred. This indicates that the axis of the reference magnetic field  $\bar{B}$  is inclined to one or the other direction of the module axis.

Furthermore, there is an obvious tendency that the intensities of the  $x$ - and  $y$ -components of the magnetic field for the non-symmetric flow rates are larger than for the symmetric case, i.e. for equal helical flow rates. Moreover, the non-symmetric cases do not achieve the same intensity values. The reason for this is not clear. It is conjectured that this effect is caused by certain structural non-symmetries in the module such as the particularities of the feed piping system connected to the module and by inhomogeneities of the seed magnetic field due to the steel structures of the laboratory building.

#### 4.3. *The effect of perturbations by external magnetic fields*

We tested the effect that an external magnetic field, generated by two Helmholtz coils, has on the dynamo magnetic field. The two coils are placed on both sides of the test module such that they can generate a unidirectional magnetic field of quasi-dipole character penetrating the module perpendicular to its axis. The coils were operated at a DC-current of 50 A and produced a nearly homogeneous magnetic field of about 20 G in the module area. For tests the power for the coils was switched on or off suddenly. Changing the current direction changed the direction of the external magnetic field.

An interesting question is: Can saturated dynamo states of opposite field direction be established by a specific perturbation of an active dynamo state with the help of an external magnetic field?

The experimental procedure for answering this question is as follows. A saturated dynamo state is first produced starting from the environmental seed field by a controlled scan up of flow rates to an intermediate level of dynamo action of, say, 20–30 G intensity. Next, by switching on the external magnetic field of opposite direction the dynamo field is destabilized and in a transient process, lasting from several seconds up to minutes, a new saturated dynamo state of opposite field direction is reached, together with the still existing external magnetic field. If the external field is switched off, a mean magnetic field of the same direction persists and a new complementary dynamo state is found. Other saturated states belonging to the same set can be generated by a suitable scan up or down of flow rates. However, the magnetic field undergoes a jump-transition to the initial dynamo state with opposite direction the magnetic field, when the volumetric flow rates fall below a lower bound of flow rates. The result of the experimental procedure outlined is displayed in figure 13. The graph shows, for a fixed central flow rate of  $\dot{V}_C = 112.5 \text{ m}^3 \text{ h}^{-1}$  and variable helical flow rates, the saturated mean value of  $y$ -components of the magnetic field  $B_y$  on a continuous branch and the complementary isolated branch of existing stationary dynamo states. Here the field component was measured by a Hall probe at the centre of the module ( $H3$ , see figure 4). This experimental observation conforms well with the theory of imperfect bifurcations from a stationary hydrodynamic state to a stationary magnetohydrodynamic state. The lowest value of the volumetric flux for the isolated branch may be identified as a turning point from which a branch of unstable, i.e. experimentally not realizable states, bifurcates for higher flow rates (for more details on bifurcation theory and hydrodynamic stability see e.g. Golubitzky & Schaeffer 1985 and Joos & Joseph 1980). Tilgner & Busse (2002) and Rädler *et al.* (2002*b*) calculated the stationary solutions of this branch as will be discussed in § 5 (see also figure 2).

Our experiments on supercritical dynamo states with field intensities larger than, say, 300 G and with perturbations by strong external magnetic fields revealed an unexpected effect. The dynamo magnetic field, enhanced by the temporary presence

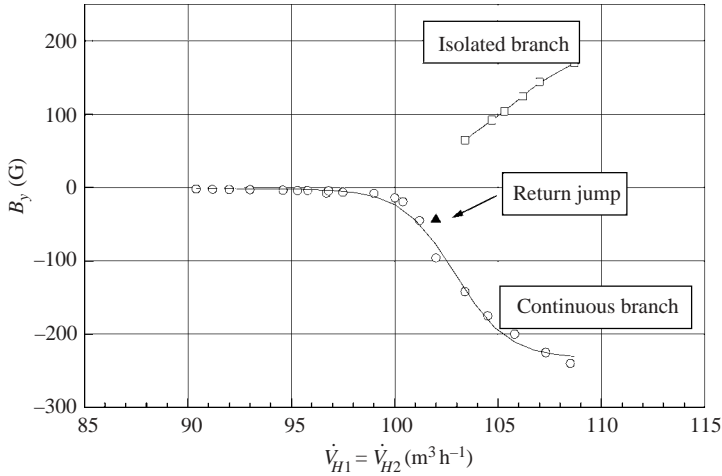


FIGURE 13. The stationary dynamo states at supercritical conditions represented by the measured local  $B_y$ -component. The graph shows two sequences of stationary states, one set on a continuous branch and another set on an isolated branch. The return jump from the isolated branch to the continuous branch is indicated by the symbol  $\blacktriangle$ . Parameter range:  $\dot{V}_C = 112 \text{ m}^3 \text{ h}^{-1}$ ,  $92 < \dot{V}_{H1,2} < 110 \text{ m}^3 \text{ h}^{-1}$ ; —, fit to experimental data.

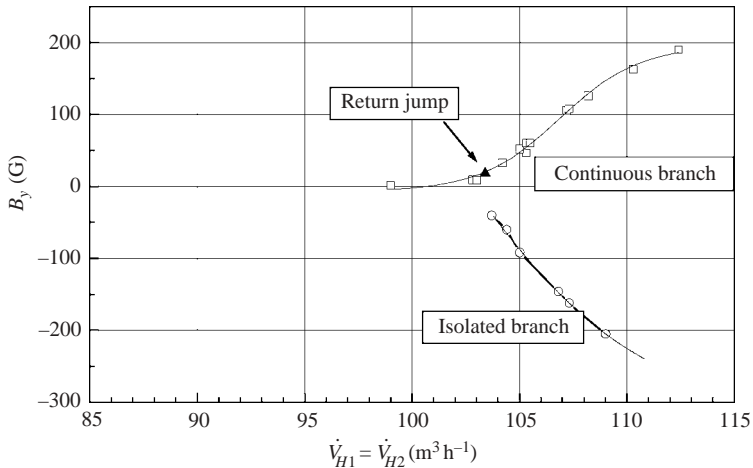


FIGURE 14. Stationary dynamo states on a continuous and an isolated branch of a bifurcation graph; however, compared to figure 13 the branches are reversed due to a modification of the environmental seed magnetic field by the dynamo magnetic field of the preceding experiment. The return jump from the isolated branch to the continuous branch is indicated by the symbol  $\blacktriangle$ . Parameter range:  $\dot{V}_C = 112 \text{ m}^3 \text{ h}^{-1}$ ,  $98 < \dot{V}_{H1,2} < 113 \text{ m}^3 \text{ h}^{-1}$ ; —, fit to experimental data.

of the external field, may noticeably influence the environmental magnetic seed field, which determines the initial conditions for the onset of dynamo action for each sequence of stepwise rising flow rates. It happened that, after an up-scan along a continuous branch of states and a termination of the test series at high field intensities, a sub-subsequent test series, starting again from low subcritical flow rates, resulted in magnetic saturation fields of opposite direction on a continuous branch. A typical example is shown in figure 14 in the form of another bifurcation graph for the  $B_y$ -component. The graph shows the continuous and the isolated branches of states.

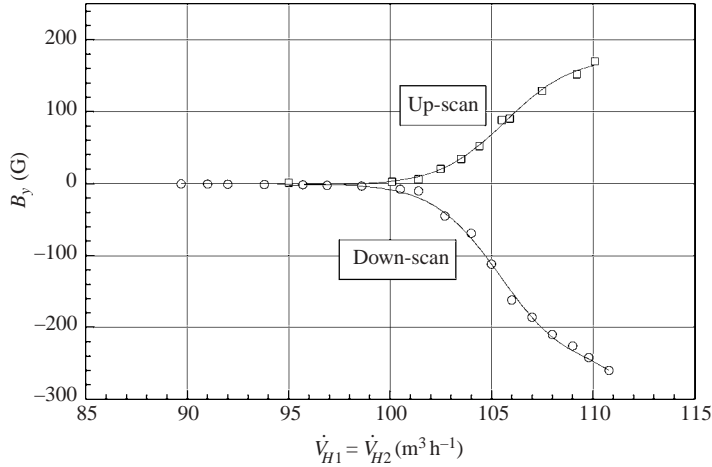


FIGURE 15. Stationary dynamo states continuously connected to hydrodynamic states for both directions of the magnetic field. The states were obtained in a monotonic up- and down-scan with a switch over to the other branch at high magnetic field intensities. It is suggested that the change of the field direction at high field intensity modifies the environmental seed field by changing the remnant weak ferromagnetism in the steel structures of the laboratory building. Parameter range:  $\dot{V}_C = 115 \text{ m}^3 \text{ h}^{-1}$ ,  $89 < \dot{V}_{H1,2} < 112 \text{ m}^3 \text{ h}^{-1}$ ; —, fit to experimental data.

The character of the complementary isolated branch could only be ensured in a test series if the transitions from the continuous to the isolated branches and vice versa are triggered by an external perturbation at an intermediate intensity level of the dynamo and the external magnetic field, say, in the range  $50 \leq |B| \leq 200 \text{ G}$ . If a transition is enforced at high intensity levels of dynamo action ( $|B| > 300 \text{ G}$ ) the complementary dynamo states of opposite direction can be scanned down in a continuous manner to vanishing field intensities. This is demonstrated in figure 15. The explanation of this behaviour must be associated with the impact of high-intensity magnetic fields on the steel structures of the laboratory building. Indeed, although the seed magnetic field level proved to be always of the order of the Earth's magnetic field, i.e.  $|B_S| \sim 0.5 \text{ G}$ , measurements with a carry-on Gauss meter showed that the orientation of the seed magnetic field inside the laboratory with the dynamo module was clearly perturbed compared to the orientation of the Earth's magnetic field measured outside the laboratory building.

Moreover, measurements of the seed magnetic field performed by traversing the Hall probe along the module axis show a distinct variation of the measured data before and after dynamo tests. This can be seen in figure 5(a, b). This observation supports our conjecture that dynamo action of high enough intensity may modify the seed field and thus result in different saturated dynamo states.

#### 4.4. Temporal features of saturated dynamo states

The saturated dynamo states are steady in the time average, but fluctuate about a mean value of the magnetic field. For characterizing these turbulent fluctuations long-term recordings of the magnetic field components ( $B_x$ ,  $B_y$ ,  $B_z$ ) of duration from 1200s up to 4800s were taken using the Hall probes. A listing of all combinations of flow rates of long-term recordings is displayed in figure 16. Here we concentrate discussions on states of equal volumetric flow rates and for constant helical flow

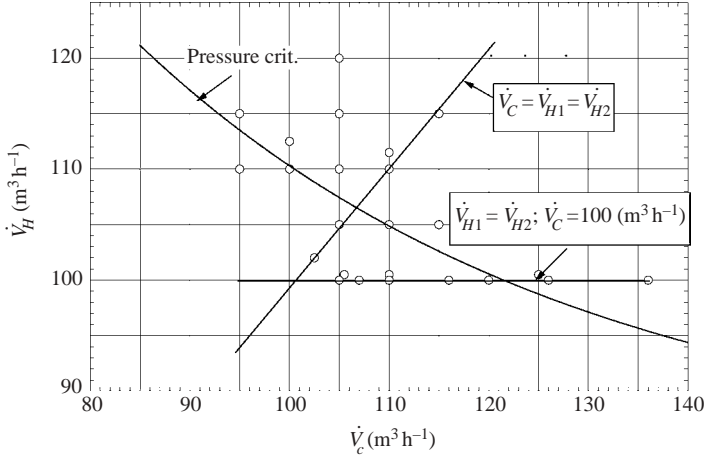


FIGURE 16. Combinations of volumetric flow rates of long-time signal recording experiments.

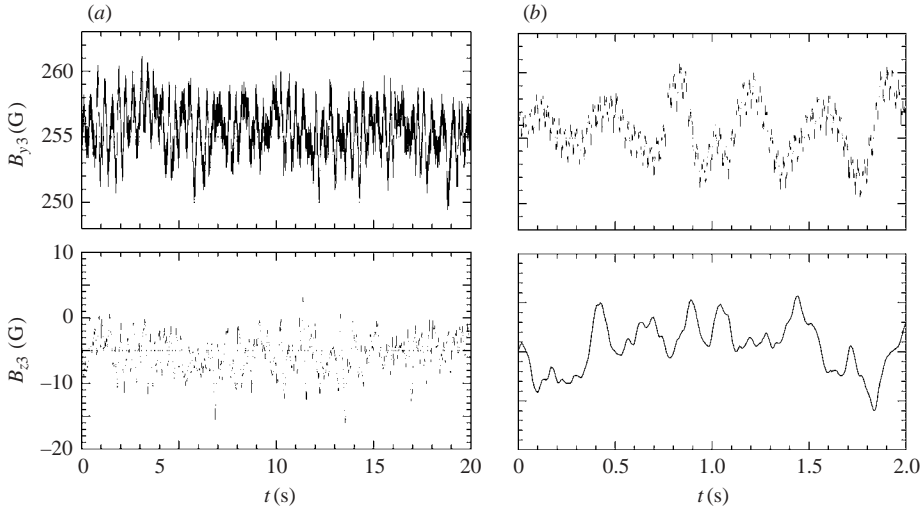


FIGURE 17. Typical time signals and two components of the magnetic field ( $B_y, B_z$ ) recorded by the Hall-probe  $H3$  for constant volumetric flow rates  $\dot{V}_C = \dot{V}_{H1,2} = 115 \text{ m}^3 \text{ h}^{-1}$  at  $z = 0$ : (a) time interval 20 s; (b) time interval 2 s.

rates as indicated by the solid straight lines in figure 16 (for other cases see Mueller, Stieglitz & Horanyi (2002)).

A typical recording for volumetric flow rates  $\dot{V}_C = \dot{V}_{H1} = \dot{V}_{H2} = 115 \text{ m}^3 \text{ h}^{-1}$  is shown in figure 17(a). An extended interval is shown in figure 17(b). From the time signal of figure 17(b) two quasi-periodic features can be seen. There are fluctuating events with frequencies of about 3 Hz and 30 Hz.

We shall identify these frequencies in the power spectral density functions (PSD) later. The quality of the fluctuations may be judged from the probability density function (PDF) and the first three moments, the standard deviation (RMS), the skewness  $S$  and flatness  $F$ . Figure 18 shows typical PDFs for the recordings in figure 17.

The associated higher moments of the  $y$ -component of the magnetic field  $B_y$  are shown in figure 19 for a recording period of 1200 s. The moments in this figure

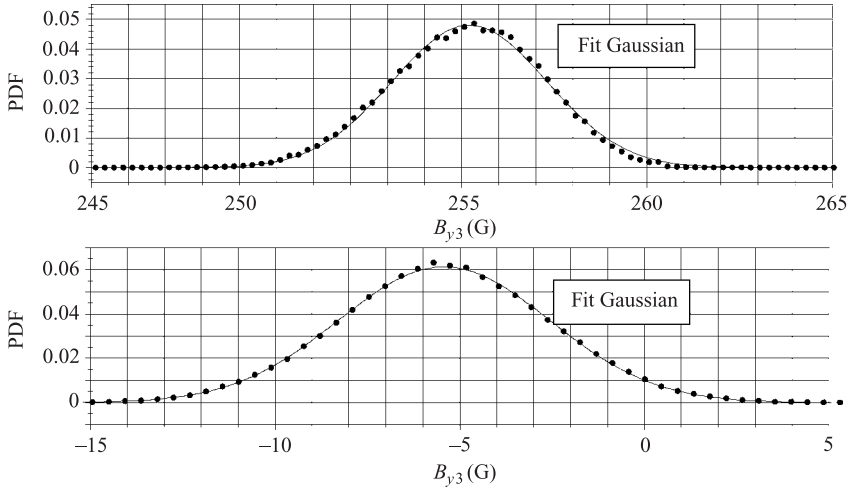


FIGURE 18. Probability density function (PDF) of the time signals of the volumetric flow rate and the two components of the magnetic field ( $B_y$ ,  $B_z$ ) of the Hall-probe  $H3$  for constant volumetric flow rates  $\dot{V}_C = \dot{V}_{H1,2} = 115 \text{ m}^3 \text{ h}^{-1}$  at  $z = 0$ .

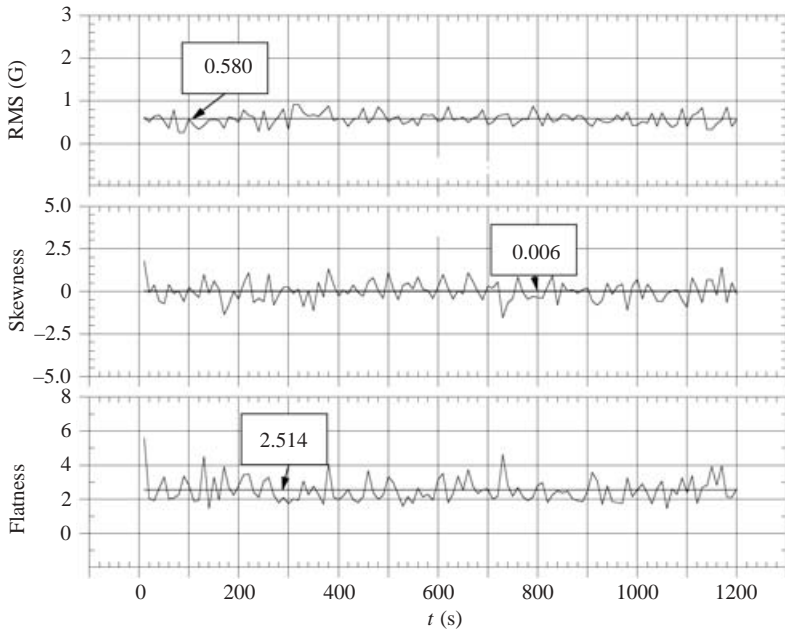


FIGURE 19. The standard deviation (RMS value), skewness and flatness values of time signal  $B_y(0, 0, 0, t)$  of Hall probe  $H3$  at  $z = 0$  for the flow rates  $\dot{V}_C = \dot{V}_{H1,2} = 115 \text{ m}^3 \text{ h}^{-1}$ .

were evaluated for periods of 10s each and for signal recording rates of 512Hz. The characteristic features are the quasi-Gaussian PDF with a vanishing skewness, a constant flatness of 2.5 and a constant standard deviation (RMS value)  $B_y^* = 0.58 \text{ G}$ . The latter has to be compared with the mean value  $\bar{B}_y = 260 \text{ G}$  which gives a small relative fluctuation level of about 0.22%. It has been observed that this level is larger for the  $z$ -component  $B_z$  and for all components near the onset of self-excitation.



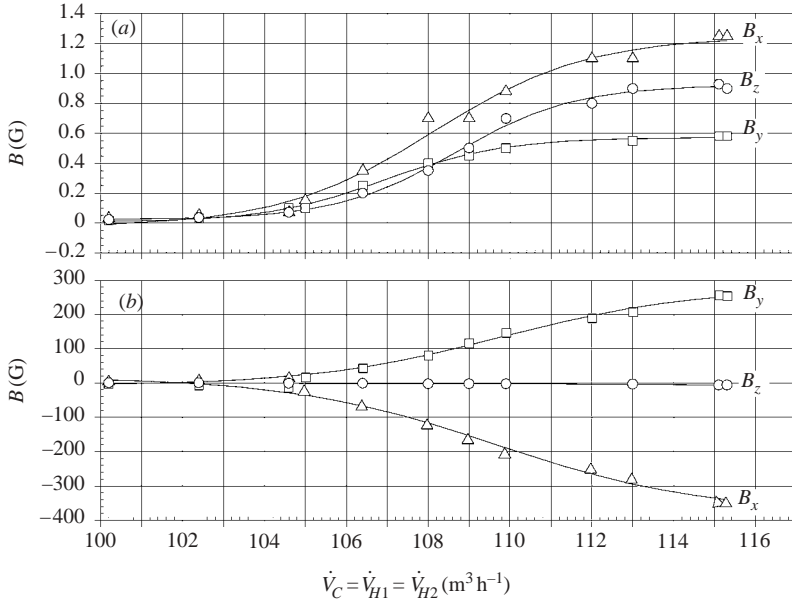


FIGURE 20. (a) The standard deviations (RMS values) and (b) the associated mean values for the time signals of  $B_x$ ,  $B_y$ ,  $B_z$  as a function of the flow rates.

Figure 19 indicates that characteristic turbulence properties are practically constant at a saturation state.

RMS values were also evaluated for other sets of equal but lower flow rates. They are shown in figure 20 together with the associated mean values of the magnetic field. The sub-linear behaviour of the RMS values  $B_x^*$ ,  $B_y^*$ ,  $B_z^*$  for higher flow rates in figure 20(a) is significantly stronger than that of the mean values in figure 20(b). In particular  $B_y^*$  and  $B_z^*$  seem to achieve saturation levels for  $\dot{V} > 112 \text{ m}^3 \text{ h}^{-1}$ . This feature can be quantified by normalizing the RMS values by the corresponding mean values. The normalized RMS values clearly decrease with increasing flow rates. From this observation we conjecture, that the increasing intensity of the mean magnetic field limits the growth rate of the turbulent fluctuations of the field.

Further insight into the character of the fluctuations is gained by considering their power spectral density (PSD). Spectra for y- and z-components of the magnetic field for five choices with equal volumetric flow rates  $\dot{V} = 95, 102, 106, 110, \text{ and } 115 \text{ m}^3 \text{ h}^{-1}$  are displayed in figure 21(a, b). Spectra for the y-component for the fixed flow rate  $\dot{V}_{H1,2} = 100 \text{ m}^3 \text{ h}^{-1}$  and for five variable central volumetric flow rates  $\dot{V}_C = 106, 116, 120, 125 \text{ and } 136 \text{ m}^3 \text{ h}^{-1}$  are displayed in figure 21(c). The spectra were obtained from long-time Hall probe recordings in the centre of the module (probe position H3, see figure 4). First we consider figure 21(a, b). According to our criterion for the onset of self-excitation, as sketched in figure 9, the flow rate  $\dot{V} = 102 \text{ m}^3 \text{ h}^{-1}$  is subcritical, the flow rate  $\dot{V} = 106 \text{ m}^3 \text{ h}^{-1}$  is about critical and the flow rates  $\dot{V} = 110 \text{ m}^3 \text{ h}^{-1}$  and  $115 \text{ m}^3 \text{ h}^{-1}$  are supercritical. The spectra of the two supercritical states show the following characteristic features: there are three distinct ranges of power distribution. There is a lower frequency range  $0.1 < f < 3 \text{ Hz}$  with nearly constant power for the  $B_z$ -fluctuations and a dependence on the frequency proportional to  $\sim f^{-1}$  for the  $B_y$ -fluctuations. In the range  $3 < f < 20 \text{ Hz}$  the spectral power decays nearly proportional to  $\sim f^{-3}$ ; and beyond this range the power decays even more rapidly, in particular

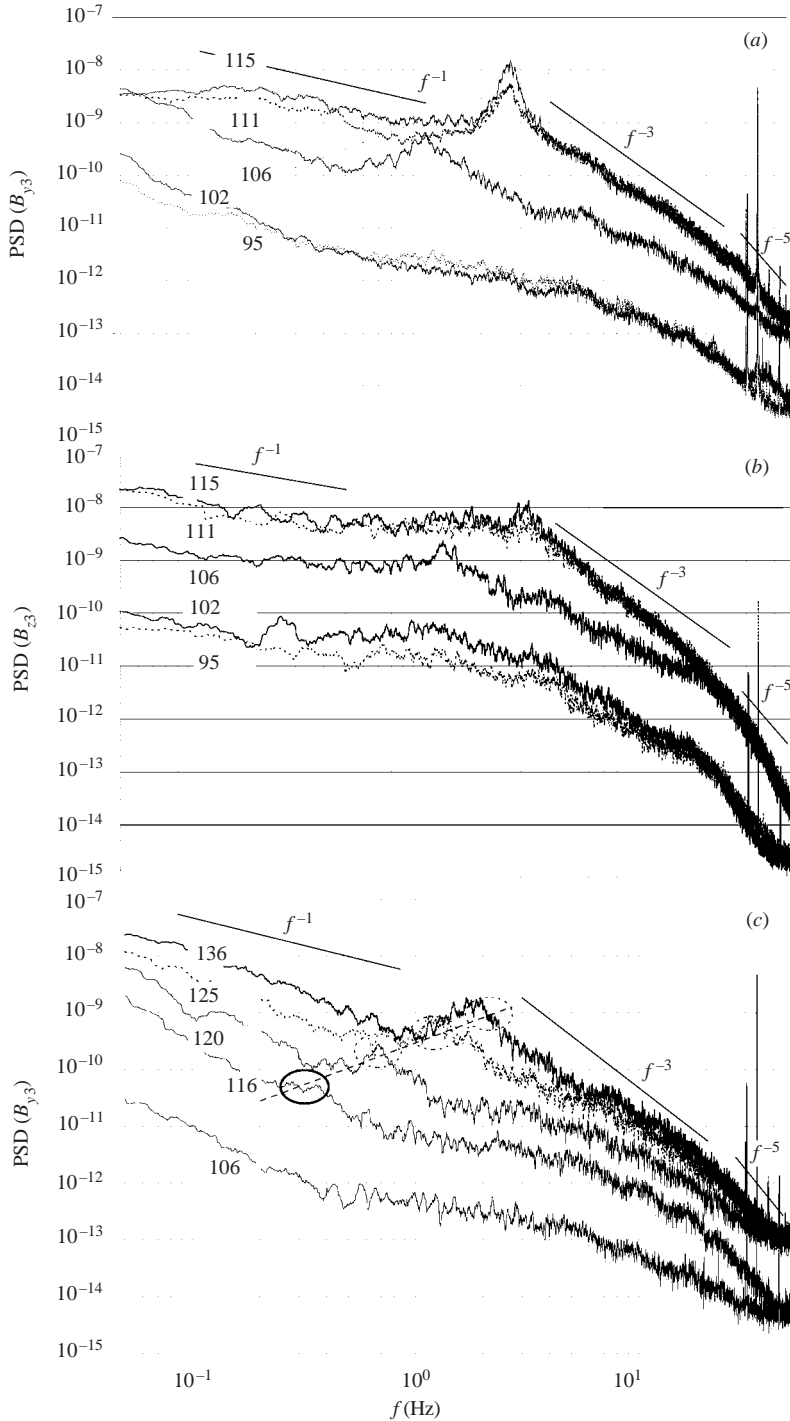


FIGURE 21. Power spectral density (PSD) for the components  $B_x$ ,  $B_y$ ,  $B_z$  for five different volumetric flow rates of operation at the position  $z=0$  of Hall probe  $H3$ . (a) PSD for the  $B_y$ -component for five equal volumetric flow rates  $\dot{V} = 95, 102, 106, 111$  and  $115 \text{ m}^3 \text{ h}^{-1}$ ; (b) PSD for the  $B_z$ -component for five equal volumetric flow rates  $\dot{V} = 95, 102, 106, 111$  and  $115 \text{ m}^3 \text{ h}^{-1}$ ; (c) PSD for the  $B_y$ -component for  $\dot{V}_{H1} = \dot{V}_{H2} = 100 \text{ m}^3 \text{ h}^{-1}$  and for five central volumetric flow rates  $\dot{V}_C = 106, 116, 120, 125$  and  $136 \text{ m}^3 \text{ h}^{-1}$ .

for the higher flow rate  $\dot{V} = 115 \text{ m}^3 \text{ h}^{-1}$ , namely nearly proportional to  $\sim f^{-5}$  or even more strongly†. The transition from the first to the second range is clearly marked by a cut-off frequency in the spectrum of the  $B_z$ -component and a broad but distinct power peak in the  $B_y$  power spectrum. The centre frequency  $f_p$  of this power peak seems to shift to lower frequencies for lower supercritical flow rates, as can be seen for the case  $\dot{V} = 106 \text{ m}^3 \text{ h}^{-1}$ . It becomes broader and less pronounced when critical conditions are approached and finally disappears for a subcritical state. In our specific case the power peak frequency reduces from 2.7 Hz to about 1.2 Hz. Similar effects are seen in figure 21(c) for volume flow rates  $\dot{V}_{H1} = \dot{V}_{H2} = 100 \text{ m}^3 \text{ h}^{-1}$  and variable flow rates  $106 \leq \dot{V}_C \leq 136 \text{ m}^3 \text{ h}^{-1}$ . For the subcritical case a broadband spectrum occurs without particular features in the  $B_y$  spectra. Under supercritical conditions typical power peaks arise whose intensities increase, while the centre frequency  $f_p$  shifts to higher values for higher central flow rates. The observations on the test sequences displayed in figure 21 were confirmed for other supercritical tests listed in figure 16.

We also conducted some experiments at subcritical volumetric flow rates under the influence of an external magnetic field of about 20 G generated by the Helmholtz coils. A typical result for the power spectral density of the magnetic field fluctuations is shown in figure 21(a) for equal flow rates  $\dot{V}_{H1} = \dot{V}_{H2} = \dot{V}_C = 95 \text{ m}^3 \text{ h}^{-1}$ . This power spectrum is comparable to the spectrum for volumetric flow rates  $\dot{V}_{H1} = \dot{V}_{H2} = \dot{V}_C = 102 \text{ m}^3 \text{ h}^{-1}$  but without an external magnetic field.

Complementary to the previous spectra recorded at the centre position we present in figure 22 some power spectra of the components  $B_y$  and  $B_z$  evaluated from signal recordings at the locations  $z = 0, 85, 175, 350 \text{ mm}$  for the case of equal volumetric flow rates  $\dot{V} = 115 \text{ m}^3 \text{ h}^{-1}$ . The spectra of the  $B_z$ -component exhibit generally a broadband behaviour with similar distinct ranges of power distribution for locations near the module centre as in the previously discussed cases, namely proportional to  $\sim f^{-1}$  in the range  $f \leq 2 \text{ Hz}$ , to  $f^{-3}$  in the range  $2 \leq f \leq 30 \text{ Hz}$  and to less than  $\sim f^{-5}$  in the range  $f > 30 \text{ Hz}$ . The spectra of the  $B_y$ -component show the characteristic power peak in the range  $f \sim 2\text{--}3 \text{ Hz}$  and for near centre positions  $z < 170 \text{ mm}$ . However, the power peak broadens and decreases with growing distance from the centre and disappears in the spectrum near the boundary of the module, i.e. towards  $z = 350 \text{ mm}$ . Simultaneously the characteristic power ranges become blurred. This behaviour is attributed to the decrease of the mean magnetic field intensity with increasing distance from the centre as can be seen in figure 11. A dependence of the characteristic frequency  $f_p$  of the power peak on the decreasing intensity of the mean magnetic field, as demonstrated in figure 21(a, c) cannot be identified in this case. The reason is as yet unclear and further investigation is needed. It is conjectured that the effect was not captured due to the lack of data recordings in the range of fast decreasing field intensities.

Dynamic regularities of the magnetic field can also be identified by evaluating cross-correlation functions (CCF) of the time signals. Cross-correlation functions can serve as a tool to detect the spatial coherency of time signals recorded at different locations. Such CCFs have been evaluated from Hall probe signal recordings. Typical sets of CCFs for time series of  $B_y$ -signals from the Hall probes  $H3$  and  $H4$  are displayed in figure 23(a–c) for the volumetric flow rate combination  $\dot{V}_C = \dot{V}_{H1,2} = 115 \text{ m}^3 \text{ h}^{-1}$ . Each figure shows five CCF graphs associated with five different positions of the

† The power spikes in the spectrum for higher frequencies  $f > 30 \text{ Hz}$  are associated with experimental noise originating from the general power supply for the test rig by the 50 Hz AC grid and the  $\approx 30 \text{ Hz}$  thyristor controlled power supply for the MHD-pumps.

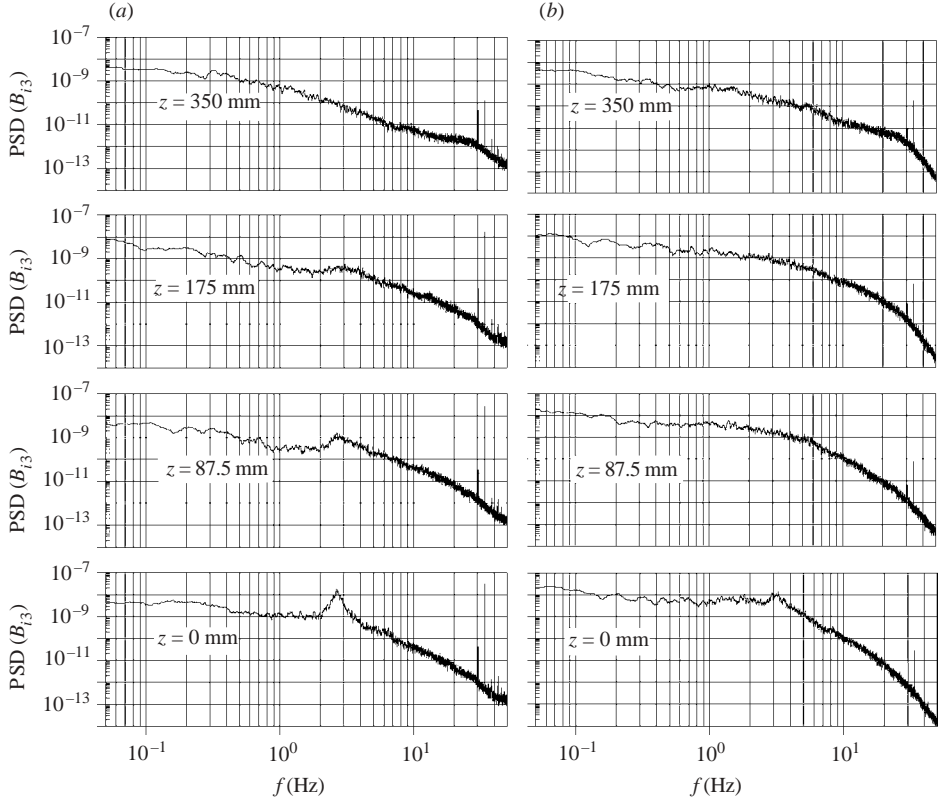


FIGURE 22. Power spectral density (PSD) of the components (a)  $B_y$ , (b)  $B_z$  of Hall probe  $H3$  for volumetric flow rates  $\dot{V}_C = \dot{V}_{H1,2} = 115 \text{ m}^3 \text{ h}^{-1}$  and at the positions  $X = (0, 0, 0)$ ,  $X = (0, 0, 87.5 \text{ mm})$ ,  $X = (0, 0, 175 \text{ mm})$ ,  $X = (0, 0, 350 \text{ mm})$ .

two probes as they are simultaneously traversed along the module axis at a constant distance of 135 mm from each other. The CCFs are presented for different time intervals ranging from  $-400 < \tau < 400 \text{ s}$  in figure 23(a) to  $-4 < \tau < 4 \text{ s}$  in figure 23(c).

The CCFs exhibit two characteristic features: (1) a stationary base caused by correlated random low-frequency events, (2) a narrowband peak of highly correlated high-frequency fluctuations. The first feature can be identified in all CCF graphs of figure 23(a) as a peaky bulge at location  $\tau = 0$  which is large and positive at the outermost position of the two probes ( $H4$  at  $z = 215 \text{ mm}$ ,  $H3$  at  $z = 350 \text{ mm}$ ) and small and even negative at the innermost position ( $H4$  at  $z = -135 \text{ mm}$ ,  $H3$  at  $z = 0$ ). The transition from the negative to the positive correlation peak at  $z = 0$  can be explained by the traversing of the two probes through a  $B_y$ -field with a maximum near the centre (see figure 11b) and a varying gradient. Accordingly the low-frequency time signals of the two probes may be in phase or out of phase, resulting in a positive and negative ‘pointed cap’ peak of the correlation curve. The time scale  $T$  of the low-frequency correlation may be estimated from the intersection of the tangent line to the cap peak with the abscissa as indicated in figure 23(a) ( $B_{y3}$ :  $z = 265.5 \text{ mm}$ ,  $B_{y4}$ :  $z = 127.5 \text{ mm}$ ). The estimate is  $T \approx 30 \text{ s}$  which corresponds to a low-frequency event of  $f \approx 0.03 \text{ Hz}$ .

The other feature, the narrowband oscillatory behaviour of the CCF near  $\tau = 0$  (which is particularly distinct for Hall probe locations near the centre of the module)

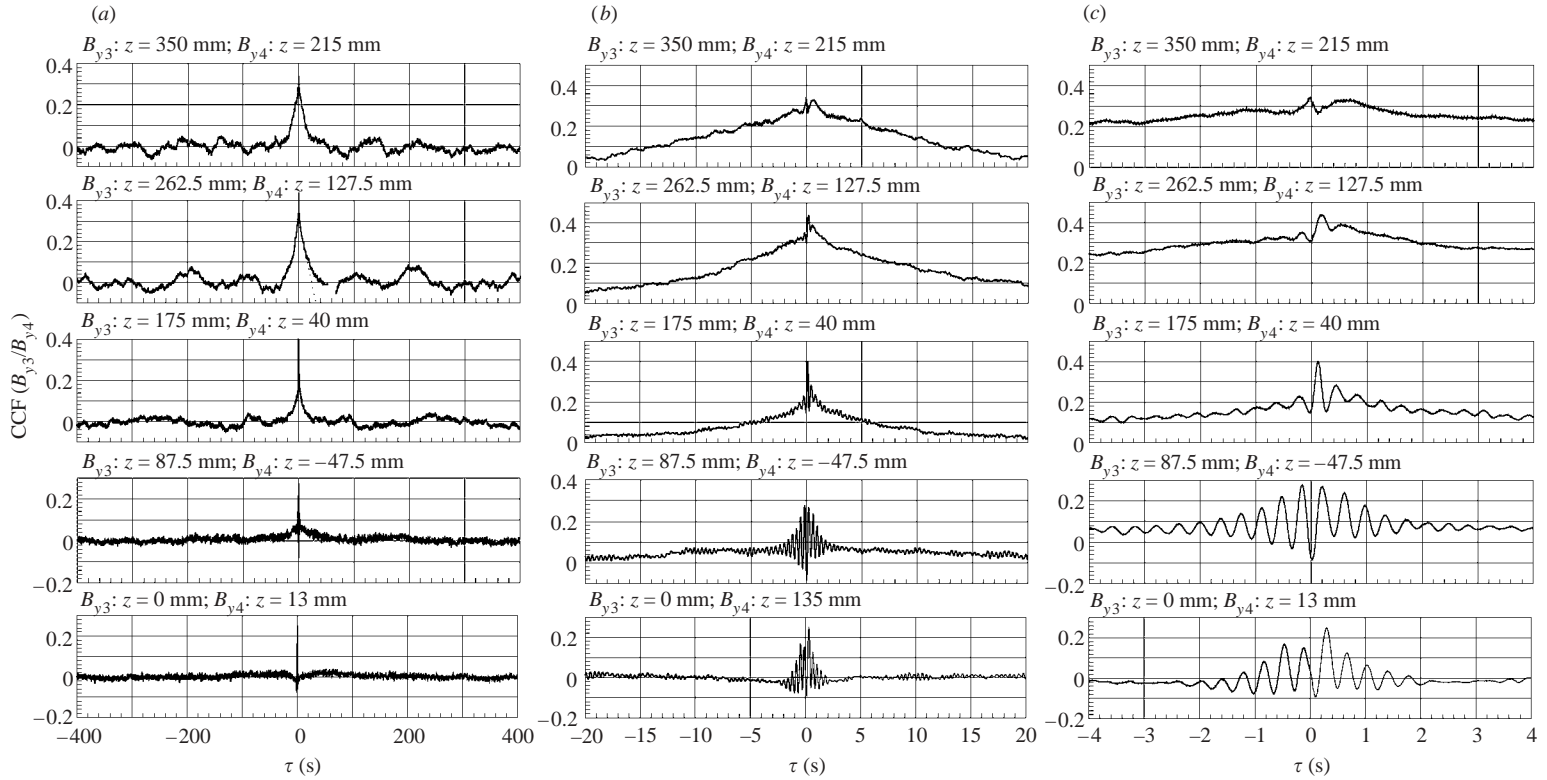


FIGURE 23. Cross-correlation function (CCF) obtained from  $B_y$ -recordings of Hall probes  $H3$  and  $H4$  at different positions on the module axis in the range  $-135 < z_{H4} < 365 \text{ mm}$ ,  $0 < z_{H3} < 350 \text{ mm}$ ; displayed time intervals: (a)  $-400 < \tau < 400 \text{ s}$ ; (b)  $-20 < \tau < 20 \text{ s}$ ; (c)  $p - 4 < \tau < 4 \text{ s}$ . Experimental condition:  $\dot{V}_C = \dot{V}_{H1,2} = 115 \text{ m}^3 \text{ h}^{-1}$ .

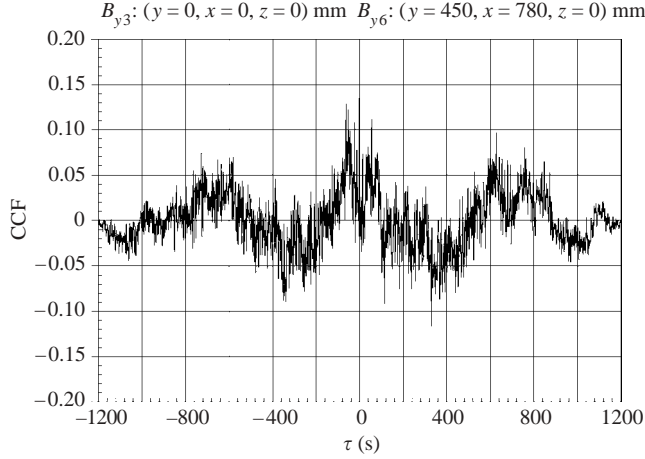


FIGURE 24. Cross-correlation function (CCF) obtained from signal recordings of Hall probes at positions  $H3$  and  $H6$ . Experimental condition:  $\dot{V}_C = \dot{V}_{H1,2} = 115 \text{ m}^3 \text{ h}^{-1}$ .

is easily seen in figure 23(b, c). The character of the CCFs in the near centre range reflects the properties of the power density spectra near their power peaks (see figure 21). The frequency of the power peak is directly related to the oscillatory period in the CCF (e.g. for  $B_{y3}$ :  $z = 0$ ,  $B_{y4}$ :  $z = -135 \text{ mm}$  one reads from figure 23(c) the value  $\tau \approx 0.3 \text{ s}$  and correspondingly in figure 21(a) the value  $f \approx 2.7 \text{ Hz}$ ). The bandwidth of the power peak in figure 21(a) is correlated to the decay time scale of the corresponding CCF. It is assessed as  $\Delta f \approx 1 \text{ Hz}$  for the case  $\dot{V} = 115 \text{ m}^3 \text{ h}^{-1}$ . The associated decay time scale (indicated in figure 23) is  $\tau \approx 1\text{--}2 \text{ s}$ .

In principle the CCFs should also indicate a transit time of wave-like events passing the spatially separated probes in a more or less regular time sequence. Indeed, for the measurements near the module centre a small signal transit time of  $\Delta\tau \approx 0.1 \text{ s}$  between the positions  $z = 0$  and  $z = -135 \text{ mm}$  may be conjectured. However, so far the evaluated CCFs have not given unbiased results for a delay time in the whole range of oscillatory behaviour of the CCF near the centre of the module. A more precise evaluation of transit times would require new Hall probe measurements with higher temporal resolution and variable spacing between the traversable sensors.

Cross-correlation measurements between Hall probes at large distance apart, i.e. between positions  $H5$  or  $H6$  and  $H3$  or  $H4$  have shown only a weak correlation of less than 10% in a very low-frequency range  $f < 0.03 \text{ Hz}$ . In all evaluated cases no delay time could be observed. This indicates that the low-frequency events occurred at both measuring positions simultaneously. A typical CCF for this kind of correlation measurement is shown in figure 24.

## 5. Discussion

In order to facilitate the discussion we have evaluated relevant magnetohydrodynamic parameters for some characteristic experimental conditions and listed them in table 1 in the Appendix. Such parameters are the fluid flow Reynolds number  $Re$  and the magnetic Reynolds number  $Rm$ , the Hartmann number  $Ha$ , the interaction parameter  $N$ , the injected mechanical helicity  $H^V$  and the mean dissipation rate  $\varepsilon$ . The quantities  $Re$ ,  $Rm$  and  $H^V$  are defined in equations (2.5) and (2.22). The Hartmann number, the interaction parameter and the dissipation rate are defined here for our

experimental conditions by the following relationships:

$$Ha = \bar{B}d_h \left( \frac{\sigma}{\rho\nu} \right)^{1/2}, \quad N = \frac{\sigma \bar{B}^2 d_h}{\rho \bar{u}}, \quad \varepsilon = \frac{1}{M} \sum_{i=1}^3 V_i \Delta p_i. \quad (5.1)$$

Here  $\bar{u}$  is the mean velocity in the helical or central channels,  $d_h$  their hydraulic diameter, and  $\bar{B}$  a measured local mean intensity of the magnetic field. For  $\bar{B}$  we shall use the measured value at the module centre (position  $H3$ ). The kinetic helicity can be evaluated, if simplifying assumptions are made for the velocity distributions in the channels. We assume that a quasi-rigid body rotation prevails in the helical channels and plug flow in the central channel. The angular velocity of the helical flow and the helicity of the total channel flow are then evaluated as

$$\Omega \approx \frac{\dot{V}_H \cos \alpha}{A_H \bar{r}} \approx \frac{\bar{u}_H}{\bar{r}} \cos \alpha, \quad H^V = \frac{\bar{u}_H^2}{\bar{r}} \sin 2\alpha, \quad (5.2)$$

where  $A_H$  is the cross-section of the helical channel,  $\bar{r}$  its mean radius and  $\alpha$  accounts for the helix pitch ( $\alpha = \arctan(h/(2\pi\bar{r}))$ ;  $h$  is the helical pitch). The total specific dissipation was evaluated using the measured volumetric flow rates  $\dot{V}_i$  in the helical and central channels, the associated measured pressure losses  $\Delta p_i$  and the total fluid mass  $M$  contained in the channel systems. Alfvén velocities  $\bar{B}/\sqrt{\mu\rho}$  based on the measured magnetic field intensity at location  $H3$  were calculated together with other parameters for experimental conditions of equal volumetric flow rates in the helical and central channels, i.e.  $\dot{V}_{H1} = \dot{V}_{H2} = \dot{V}_C$ , and are listed in table 1, together with data for conditions of constant helical but variable central flow rates. The table shows that the volumetric flow rates realized correspond to high Reynolds numbers on the one hand, but result in low magnetic Reynolds numbers on the other. In figure 9 the phase diagram for dynamo action is also displayed as a function of magnetic Reynolds numbers for the helical and central flow.

Apart from the magnetic Reynolds number, two other magnetohydrodynamic groups, the Hartmann number  $Ha$  and the interaction parameter  $N$ , may characterize the dynamo in the supercritical range. It is seen in the table that the Hartmann number can achieve a considerable value of up to  $Ha = 500$  at the highest supercritical flow rates, and it still has values of  $Ha = 20$  at near critical conditions. It is well known from channel flow that the fluid dynamic velocity profile is subjected to significant deformation by Lorentz forces at Hartmann numbers of the order  $Ha = 20$ . This is certainly the case in the channel system of the dynamo module at supercritical saturated dynamo states. The significant increase in the pressure drop is an obvious sign of the deformation of the velocity profile by Lorentz forces and dissipative Joule losses. Moreover, it is to be expected that turbulent fluctuations in the high-Reynolds-number channel flow are strongly damped by the dynamo mean magnetic field according to its intensity distribution in the module. This conjecture is supported by the size of the interaction parameter  $N$ , of order 1 at the higher volumetric flow rates. As the interaction parameter can be considered a measure of the ratio of the vortex turn-over time and the Joule dissipation time of a vortex that is the size of the channel diameter (cf. Alemany *et al.* 1979), even the largest possible fluctuations experience significant Joule damping. The dissipative destruction of smaller vortices is certainly stronger. Thus, a tendency to partial relaminarization of the channel flow may be expected. This conjecture is substantiated by the saturation behaviour of the RMS-values at supercritical conditions, as is seen in figure 20.

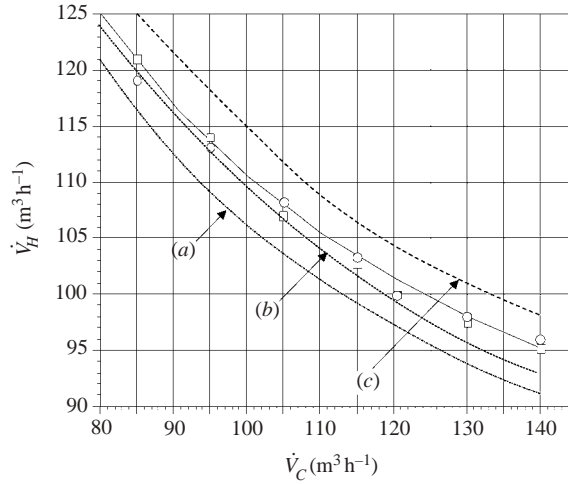


FIGURE 25. Phase diagram for dynamo action in the Karlsruhe dynamo experiment as a function of the different flow rates. Comparison between experiment and model calculations of Tilgner (2002). The continuous line corresponds to a magnetic diffusivity  $\lambda_{eff} = 0.1 \text{ m}^2 \text{ s}^{-1}$  and an aspect ratio  $D/r_0 = 1.2$ . The dotted line (b) is for  $\lambda_{eff} = 0.11 \text{ m}^2 \text{ s}^{-1}$  and  $D/r_0 = 1$ . The lines (a) and (c) show results for  $D/r_0 = 1$ , different magnetic diffusivities  $\lambda_{eff} = 0.11 \text{ m}^2 \text{ s}^{-1}$  (a),  $\lambda_{eff} = 0.115 \text{ m}^2 \text{ s}^{-1}$  (c) and a slightly modified velocity profile.

The self-excitation of the dynamo has been defined in §4.1 according to experimental criteria. These findings have been confirmed by model calculations of Tilgner (2002) and Rädler *et al.* (2002a). Figure 25 shows for comparison the experimental data and the calculated curves of Tilgner (2002) in the dynamo phase diagram. In Tilgner's calculations an effective magnetic diffusivity  $\lambda_{eff}$  has been used which takes into account a correction of molecular magnetic diffusivity  $\lambda$  due to turbulent motion and a reduced average molecular conductivity due to the stainless steel piping structures in the module. He also tested the sensitivity of the marginal states to slight variations of the geometry of the dynamo module (the aspect ratio) and to variations of the velocity distribution in the vortex generator. The details are described in the figure caption. The agreement between experiment and model calculation is adequate. Rädler *et al.* (2002a) have obtained similar results (see their figure 15 and their evaluation of the additional turbulent diffusivity).

The overall structure of the observed magnetic field mode, as displayed in figure 10(a, b), is in good agreement with the predictions of the model theories of Tilgner (1997, 2002) and Rädler *et al.* (2002a). Both model theories predict a quasi-dipolar magnetic field of the mode type  $m = 1$  as realized in the experiment. Indeed, Tilgner (2002) calculated an isoline graph of the magnetic field, which conforms to the measured isoline field of figure 10(a). There are, however, discrepancies between theoretical predictions and measurements concerning the local structure of the magnetic field. For equal helical flow rates the theory gives a twisting of the radial magnetic field vectors by an angle  $\pi$  for positions along the cylinder axis. The experimental measurements indicate an angle of  $\pi/2$  only, as is seen from figure 11(b, d). Another striking observation is the deviation of the measured distribution of the magnetic field components on the module axis. Although the measurements were taken only on the semi-axis  $0 < z < 350 \text{ mm}$ , there are qualitative deviations from the symmetries predicted by theory. This is seen from figure 26 which is a not-to-scale reproduction



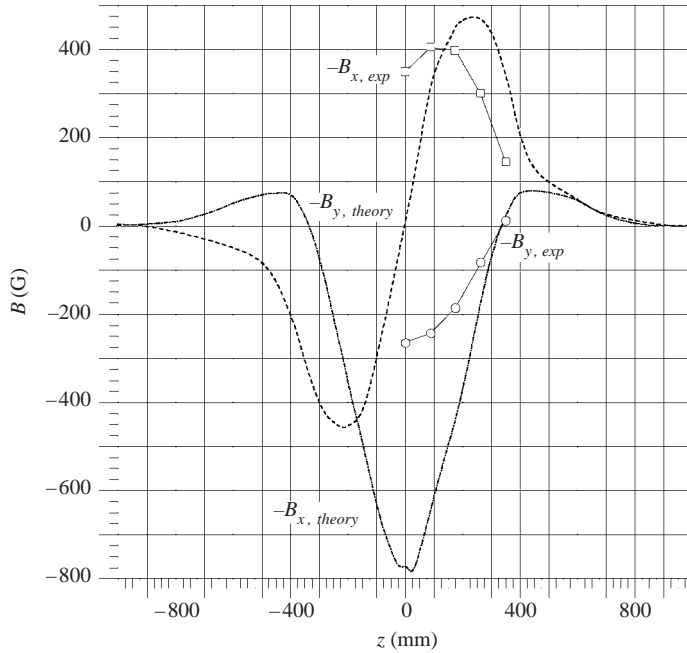


FIGURE 26. The calculated distribution of the  $B$ -field components on the module axis ( $x = y = 0$ ) after Rädler *et al.* (2002a), displayed as dashed and dashed-dotted lines for the flow rates  $\dot{V}_C = \dot{V}_{H1,2} = 115 \text{ m}^3 \text{ h}^{-1}$ ,  $\lambda = 0.1 \text{ m}^2 \text{ s}^{-1}$ . The experimental results correspond to figure 4.6a and are denoted by symbols  $\square$  and  $\circ$ .

of figure 6 of Rädler *et al.* (2002a) in which the experimental curves of figure 11(a) are roughly integrated. The measured field components  $B_{x,exp}$  and  $B_{y,exp}$  were phase shifted by an angle  $\beta = 3/2\pi$  to be comparable with the calculated symmetric and anti-symmetric components. It is as yet unclear what causes this non-symmetric behaviour of the dynamo magnetic field, which results in the experimental observations.

The weakly nonlinear behaviour of the Karlsruhe dynamo in the supercritical regime is best characterized as an imperfect bifurcation of the magnetohydrodynamic state from a pure hydrodynamic state of helical channel flow. Although the kind of bifurcation has been identified from local field measurements only (see figures 13, 14), one may presume that the spatially averaged intensity of the magnetic field would show the same behaviour. The experimental results suggest that the smooth transition from the non-magnetic to a magnetic state is determined by the initial distribution of the seed field and, moreover, that this initial condition is subjected to changes that depend on the intensity and duration of the action of the dynamo magnetic field on the structural environment of the test module. There is yet another permanent feature of the magnetic field generated by this test module: the intensity of the magnetic field component  $B_y$  is stronger at high supercritical conditions, if its orientation is in the negative  $y$ -direction (see figure 13 compared to figure 14). This again indicates a systematic structural non-symmetry of the test facility and, even more important, the influence of the environment in the laboratory which contains ferromagnetic structural material such as steel beams and floors.

Tilgner & Busse (2002) and Rädler *et al.* (2002b) developed models to describe dynamo action in the slightly trans-critical regime. They find an imperfect bifurcation for the transition to dynamo action that depends on the orientation of an initial

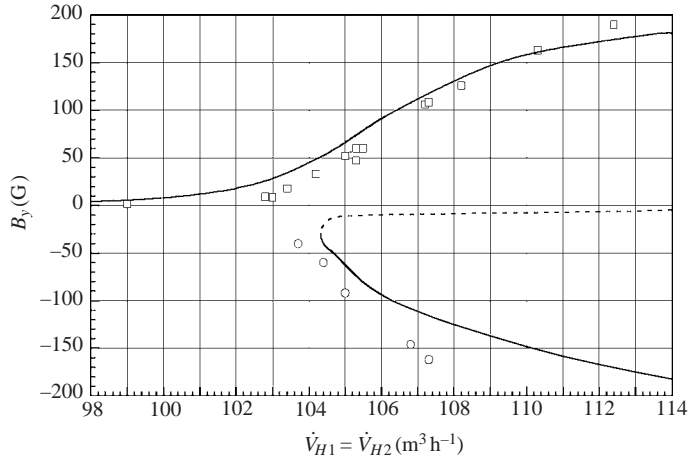


FIGURE 27. The magnetic field component  $B_y$  at the centre of the test module as a function of equal helical volumetric flow rates  $\dot{V}_{H1,2}$  for a fixed central flow rate  $\dot{V}_C = 112 \text{ m}^3 \text{ h}^{-1}$ . The symbols  $\circ$ ,  $\square$  indicate the experimental results as presented in figure 14. The continuous and the dashed lines are solutions for this parameter set obtained by Rädler *et al.* (2002b).

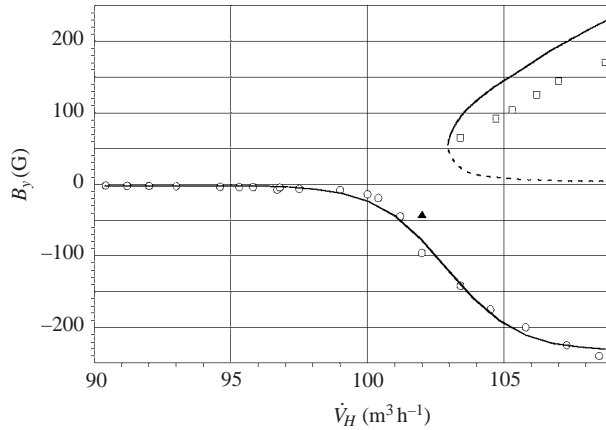


FIGURE 28. The magnetic field component  $B_y$  at the centre of the test module as a function of equal helical volumetric flow rates  $\dot{V}_{H1,2}$  for a fixed central flow rate  $\dot{V}_C = 112 \text{ m}^3 \text{ h}^{-1}$ . The symbols  $\circ$ ,  $\square$  indicate the experimental results as presented in figure 13. The continuous and the dashed lines are solutions of the steady state of model equation (2.7) with  $Rm$  replaced by  $\dot{V}_{H1,2}$  and  $\dot{V}_{crit} = 102 \text{ m}^3 \text{ h}^{-1}$ ,  $B_0 = -0.5 \text{ G}$  and  $c/\beta = 9 \times 10^3 \text{ G}^2 \text{ h m}^{-3}$  according to Tilgner & Busse (2002).

seed field and thus confirm the overall observation. There is however a quantitative difference between the predicted and the measured intensities of the isolated branch. As a demonstration we compare our results with calculations of Rädler *et al.* (2002b) in figure 27. The experimental data correspond to those in figure 14. The calculations of Rädler *et al.* are based on a mean field approach.

Tilgner & Busse (2002) arrived at equivalent results using spectral numerical and low-order analytical methods. Their results are displayed together with the data of figure 13 in figure 28. Their model equation (2.7) suggests that the saturation of the magnetic field to a steady state is achieved by a reduction of the *amplification*

coefficient  $[(Rm/Rm_c - 1) - (\beta/Rm_c)|\bar{B}|^2]$  caused by the action of Lorentz forces which is reflected in the term  $(\beta/Rm_c)|\bar{B}|^2$ .

In general it can be stated that the theoretical predictions based on independent mathematical procedures are in good agreement with the observations and measurements, except for certain structural non-symmetries of the test module that are not represented and except for some differences between the local measurements of the field intensity and the calculated mean values for the magnetic field. This is not surprising, as the calculations are based on a smoothing approximation using small-scale spatial averaging.

The Gaussian character of the probability distribution of the fluctuations of the magnetic field components in figure 18 suggests that the turbulent hydromagnetic processes may be locally quasi-isotropic. This is corroborated by the vanishing skewness factor and a flatness factor of 2.5, which is close to the Gaussian value 3. Compared to the intensity of the mean magnetic field, the intensities of the fluctuations, measured by the RMS value, are small, of order less than 1% and, moreover, the relative level seems to decrease for growing mean field intensity (see figure 20). This indicates enhanced Joule dissipative damping for the small-scale hydromagnetic turbulence.

The power spectra of the magnetic field fluctuations, displayed in figures 21 exhibit the following general features: The power level increases in the whole spectral range with increasing intensity of the local mean magnetic field. For active dynamo states of more than about 50 G the PSD functions of the  $B_y$ -components show a pronounced broad peak whose centre frequency  $f_p$ , as introduced in §4.4, increases with the increasing intensity of the local mean magnetic field. It varies for our experimental conditions roughly in the range  $1 < f < 3$  Hz (see figure 21a). The other two field components do not show a similarly distinct power peak. However, the  $B_z$ -component indicates a cut-off frequency in the range  $1 < f < 3$  Hz which separates a range of quasi-constant power spectra from the range of decaying power spectra.

The functional character of the power spectra may be discussed in the light of spectral models for magnetohydrodynamic turbulence and dynamo theory, as outlined in §2.4. The discussion is based on the premise that Taylor's hypothesis holds and the measured frequencies can be directly correlated to wavenumbers (see §2.4).

We may roughly distinguish three characteristic functional ranges in the power spectra of the  $B_y$ -component for strong dynamo action: the low-frequency range  $f < f_p$  with a PSD  $\sim f^{-1}$  behaviour the range  $f > f_p$  with a PSD  $\sim f^{-3}$  dependence; and a high-frequency range  $f \geq 20$  Hz with PSD  $\sim f^{-5}$ . There seems to be a constant saturation level for frequencies  $f < 0.1$  Hz for the most intensive dynamo states (see figure 21a). The suggested functional relationships for the different ranges are based on relevant spectral models for MHD turbulence in the literature.

The PSD  $\sim f^{-1}$  relationship in the low-frequency range seems to support the theoretical findings of Pouquet *et al.* (1976), who discovered a reverse energy cascade for a dynamo driven by an injection of helicity into the system at a particular frequency  $f_{in}$  which is beyond the reverse cascade range. We have evaluated this injection frequency for the helicity (see tables 1 and 2) and find that it is practically constant for all our experimental conditions. Furthermore, it is larger by more than a factor 2 than the power peak frequencies  $f_p$ .

We note here that Marie *et al.* (2001) and Peffley, Cawthorne & Lathrop (2000) also observed a frequency range PSD  $\sim f^{-1}$  in their power spectra obtained from their experiments with swirling flows in closed containers and imposed external magnetic fields. However, these authors do not observe power peaks in their spectra. We thus conjecture that the presence of such peaks in our spectra is associated

with dynamo action in our experiments. Moreover, whether all these independent experimental observations can be explained by the Pouquet *et al.* (1976) theory is not obvious and needs further elaboration.

The spectral decay of the field intensity in the frequency range  $f > f_p$  may be attributed to a non-dissipative cascading process of energy towards higher wavenumbers by local or non-local Alfvén wave interaction with a weak or strong correlation between the velocity and the magnetic field (see Grappin *et al.* 1983). This mechanism results in decay functions  $\text{PSD} \sim f^{-m}$ , with  $3/2 < m < 3$  as outlined in §2.4 (see equation (2.13) and (2.14)). The character of the power spectra in figure 21(a) seems to support this model in the relevant range  $f_p < f < f_{K\lambda} < 15\text{ Hz}$  with  $f_{K\lambda}$  as the Kolmogorov frequency (see also table 1).

For the high-frequency range the high Hartmann numbers as well as the size of the interaction parameter  $N$ , of order  $O(1)$  for intensive dynamo action, suggest that the decay is predominantly governed by Joule dissipation in the stagnant fluid zones and in the bulk flow by current short circuits in the free eddies of the turbulent flow. The Kolmogorov Joule dissipation time scale defined in equation (2.9) in §2.4 gives the threshold frequency  $f_K$  beyond which Joule dissipation would dominate the spectral distribution. This is evaluated in table 1 in the Appendix. It varies roughly between 10 and 15 Hz in experiments of significant dynamo action†. Thus, following Moffatt (1961) the spectral decay of the magnetic field fluctuations should vary in the frequency range  $f > f_{K\lambda}$  between  $\text{PSD} \sim f^{-11/3}$  and  $\text{PSD} \sim f^{-5}$  depending on the spectral energy distribution of the turbulent velocity fields which may be of the order  $E_f^V \sim f^{-5/3}$  or  $\sim f^{-3}$  (see equations (2.12) and (2.15)). The experimental observation according to figure 21(a–c) is that there is certainly a steeper decrease of power in the spectra for frequencies  $f > 20\text{ Hz}$  which may be described by rates  $-5 < m < -11/3$  depending on the intensity of the mean magnetic field. Thus, the observed dissipative decay of the experimental spectra seems to be compatible with the picture of dissipative MHD turbulence in the frequency range  $f > f_{K\lambda}$ .

It may be conjectured that the location of the peaks in the power spectra of intensive dynamo action may correlate with the injection frequency of kinetic helicity into the dynamo module. This injection frequency  $f_{in}$  is roughly defined by relationship (5.2). However, the evaluation of these frequencies for the typical experiments listed in table 1 gives values between  $4.2 < f_{in} < 4.7\text{ Hz}$  and  $5.3 < f < 5.9\text{ Hz}$  respectively. This is a frequency range which is about twice as high as the observed location range of the power peaks between  $0.7 < f < 3\text{ Hz}$  (cf. figure 21a, c). Moreover, the experimental range of injection frequencies is considerably smaller, as its variation depends essentially on the experimentally realized volumetric flow rates. There is no obvious correlation between the two frequencies  $f_p$  and  $f_{in}$ . Thus, a scaling of the power peak frequency  $f_p$  with the kinetic helicity injection frequency seems to be inadequate. A more suitable time scale for the frequency  $f_p$  seems to be the transit time of an Alfvén wave along the ‘structural wavelengths’ of the module, which is  $L = 2a$ . The corresponding frequency scale is  $f_A \approx V_a/2a$ . In table 1 in the Appendix these frequencies are evaluated for relevant cases. The frequencies of the power peaks in the spectra agree fairly well with the reciprocal transit times of the Alfvén waves along the characteristic structural length scale  $L = 2a$ , i.e. two diameters of a vortex generator. Therefore, we suggest that the power peaks in the power density spectra

† The corresponding Kolmogorov length scale has also been evaluated for the considered cases. It varies in the range 0.08–0.105 m and is thus of the order of the hydraulic diameters of the channels of the vortex generators (see table 1).

reflect a resonant interaction of Alfvén waves with the smallest possible wavelength associated with the smallest structural length scale  $a$  of the module. This conjecture is supported by the cross-correlation measurements (see figures 23 and 24) which show that the high-frequency signals are strongly correlated at short distances of two Hall probes, but are uncorrelated at distances of the module's dimension. Moreover, the correlation function for the high-frequency signals indicate a delay time, while the low-frequency correlations for large distances of the probes do not. This is not surprising in the light of the theory of Alfvén waves, since even for the most intensive dynamo actions in our experiments Alfvén waves are dampened in liquid sodium on length scales of about 0.1 m. It may thus be questioned whether the oscillatory features of the magnetic field should be associated with the phenomena of linear Alfvén wave propagation (cf. Davidson 2001), as these waves are strongly damped in liquid sodium. However, at super-critical conditions there is the possibility of nonlinear interactions of damped waves, which may lead to sustained finite-amplitude waves. In this context Grappin *et al.* (1983) speak of 'Alfvénic fluctuations' and 'Alfvénic turbulence'.

## 6. Conclusions and perspectives

The Karlsruhe dynamo experiment has demonstrated that a permanent magnetic field of considerable intensity can be generated spontaneously by a regular arrangement of stationary vortices in a conducting fluid. The saturation of the magnetic field is achieved by the feedback of the magnetic field onto the velocity distribution as suggested by the dynamo model of Tilgner & Busse (2002) as well as that of Rädler *et al.* (2002*b*). The experimental findings concerning the linear and weakly nonlinear behaviour of the dynamo agree on the whole with the model predictions. The other characteristic property of the dynamo magnetic field is the turbulent fluctuations of the field about its mean value. The statistical properties of these fluctuations fit the scope of predictions from MHD turbulence models available in the literature.

Although one may conjecture that these fluctuations of the magnetic field correlate with the velocity fluctuations of the turbulent channel flow, direct measurements were not performed, as velocity measurements, in particular velocity fluctuation measurements, in liquid metal flow are difficult and tedious. Further experiments with adequate instrumentation for velocity measurements should corroborate our conjectures for the velocity spectra and also confirm the feedback of the dynamo magnetic field onto the mean velocity and the velocity fluctuations.

The Karlsruhe dynamo experiment could not have been performed without the continuous support of this project by the executive board of the Forschungszentrum Karlsruhe. The authors gratefully acknowledge this support. They would like to thank the technical staff of the Institut für Kern- und Energietechnik, E. Arbogast, V. Krieger, W. Liebel, K. Marten, J. Meinel, P. Miodek, F. Nikolaus, D. Rackel, D. Schlindwein for their excellent technical assistance during the construction of the test facility and its operation. They are indebted to their colleagues, L. Barleon, L. Bühler, H. Hoffmann, J. Reimann for fruitful discussions and technical advice. Theoretical input to the experimental dynamo program was continuously provided by F. Busse and A. Tilgner of the University of Bayreuth and K.-H. Rädler and his colleagues of the Astrophysikalisches Institut Potsdam. Their theoretical support has been extremely valuable for the success of the experiment.

$\bar{V}_C$ [m <sup>3</sup> h <sup>-1</sup> ]	$\bar{V}_H$ [m <sup>3</sup> h <sup>-1</sup> ]	$Re_C$	$Re_H$	$ B^2 $ [G <sup>2</sup> ]	$Ha_C$	$N$	$\Omega_m$ [s <sup>-1</sup> ]	$\epsilon_{int} = M^{-1} \sum_i V_i \Delta p_i$ [m <sup>2</sup> s <sup>-3</sup> ]		$f_{in} = \frac{\Omega}{2\pi}$ [s <sup>-1</sup> ]	$V_a = B(\rho\mu)^{-1/2}$ [m s <sup>-1</sup> ]
$\bar{u}_C$ [m s <sup>-1</sup> ]	$\bar{u}_H$ [m s <sup>-1</sup> ]	$Rm_C$	$Rm_H$	$ B $ [G]			$H^V = 2\Omega\bar{u}_H \sin\alpha$ [m s <sup>-2</sup> ]	$f_{K\lambda} = \left(\frac{\lambda}{r}\right)^{1/2}$ [s <sup>-1</sup> ]	$L_{K\lambda} = \left(\frac{\lambda^3}{r}\right)^{1/4}$ [m]	$f_{in}^* = \frac{\dot{\alpha}}{\dot{\alpha}_0}$ [s <sup>-1</sup> ]	$f = V_a(2a)^{-1}$ [s <sup>-1</sup> ] $2a = 0.42$ [m]
115	115	$6.7 \times 10^5$	$4.7 \times 10^5$	$2.2 \times 10^5$	590	0.55 <sub>C</sub>	37	21.7		5.9	1.37
4.1	3.1	4.03	2.83	$4.7 \times 10^2$		0.73 <sub>H</sub>	82	14.7	0.082	4.7	3.3
111	111	$6.5 \times 10^5$	$4.2 \times 10^5$	$2.15 \times 10^5$	573	0.56 <sub>C</sub>	35			5.6	1.35
3.9	3.0	3.89	2.52	$4.6 \times 10^2$		0.74 <sub>H</sub>	75			4.5	3.2
106	106	$6.3 \times 10^5$	$4.0 \times 10^5$	$2.4 \times 10^4$	187	0.07 <sub>C</sub>	33	8.23		5.25	0.44
3.8	2.8	3.75	2.39	$1.5 \times 10^2$		0.09 <sub>H</sub>	66	9.1	0.105	4.2	1.04
102	102	$6.0 \times 10^5$	$3.8 \times 10^5$	$4.5 \times 10^2$	26	$1.3 \times 10_C^{-3}$	31			4.9	0.06
3.6	2.7	3.6	2.28	$2.1 \times 10^1$		$1.7 \times 10_H^{-3}$	60			4.1	0
95 <sup>(1)</sup>	95	$5.6 \times 10^5$	$3.3 \times 10^5$	$5.0 \times 10^2$	27	$1.5 \times 10_C^{-3}$	29			4.6	0.06
3.4	2.5	3.36	2.00	$2.2 \times 10^1$		$2.1 \times 10_H^{-3}$	52			3.8	0
135	100	$7.9 \times 10^5$	$5.6 \times 10^5$	43000	253	0.09 <sub>C</sub>	32	14		5.1	0.61
4.8	2.7	4.73	2.46	207.3		0.16 <sub>C</sub>		12	0.091		1.45
126	100.5	$4.5 \times 10^5$	$4.1 \times 10^5$	24000	195	0.05 <sub>C</sub>	32	11.04		5.1	0.45
4.5	2.7	4.42	2.47	155		0.09 <sub>H</sub>					1.07
120	100.5	$7 \times 10^5$	$4.1 \times 10^5$	6700	103	0.02 <sub>C</sub>	32	9.6		5.1	0.24
4.3	2.7	4.20	2.47	82		0.03 <sub>H</sub>		9.8	0.101		0.57
116	105.5	$6.8 \times 10^5$	$4.1 \times 10^5$	1500	49	$4 \times 10_C^{-3}$	32			5.1	0.11
4.1	2.7	4.06	2.47	39		$6 \times 10_H^{-3}$					0.26
110	105.5	$6.4 \times 10^5$	$4.1 \times 10^5$	135	15						
3.9	2.7	3.52	2.47	11.6							

<sup>(1)</sup> with external magnetic field  $B \approx 25$  [G]

TABLE 1. Characteristic numbers of the Karlsruhe Dynamo experiment during operation.

The members of the Karlsruhe Dynamo Project Council, W. Deinzer from the University of Göttingen, M. Proctor from the University of Cambridge, UK, K.-H. Rädler from the Astrophysikalisches Institut Potsdam, M. Stix from the Kiepenheuer Institut für Sonnenphysik in Freiburg deserve our special thanks for their positive valuation of the experimental program and their constructive comments during the early phase of the research project.

Finally, the authors thank the Deutsche Forschungsgemeinschaft for a financial support of Sandor Horanyi for his evaluation of the large experimental data sets.

## Appendix

The table in this appendix lists magnetohydrodynamic parameters for some characteristic experimental conditions. The data are arranged as follows. They are ordered by the central and helical flow rates  $\dot{V}_C$  and  $\dot{V}_H$  and the associated mean velocities  $\bar{u}_C$  and  $\bar{u}_H$  in the first two columns. There are two sets of data, one for equal central and helical flow rates, the other for non-equal ones. The data associated with each pair of flow rates are arranged in double lines where the first two lines list the related symbols or definitions. Other relevant definitions are given below:

$$P_m = \nu/\lambda \approx 6 \times 10^3; \quad d_{hC} = a/2; \quad A_C = \pi/4(D_L)^2 = 0.78 \times 10^{-2} [\text{m}^2];$$

$$d_{hH} = \frac{h}{2(h/a + \frac{1}{4})} \approx \frac{2}{5}h; \quad A_H = ah/4; \quad \Omega = (\bar{u}_H/\bar{r}) \cos \alpha;$$

$$\alpha = \arctan(h/2\pi\bar{r}); \quad V_D = \lambda/(2a) = 0.25 [\text{m s}^{-1}];$$

$$Ha = d_h B(\sigma/\rho\nu)^{1/2}; \quad N = \sigma|B|^2 d_h/(\rho\bar{u}_{C,H}).$$

## REFERENCES

- ALEMANY, A., MOREAU, R., SULEM, P. L. & FRISCH, U. 1979 Influence of an external magnetic field on homogeneous MHD turbulence. *J. Méc.* **18**, 277–313.
- AUBERT, J., BRITO, D., NATAF, H. G., CARDIN, P. & MASSON, J. P. 2001 A systematic experimental study of rapidly rotating spherical convection in water and liquid gallium. *Phys. Earth Planet. Inter.* **128**, 51–74.
- BISKAMP, D. 1993 *Nonlinear Magnetohydrodynamics*. Cambridge University Press.
- BISKAMP, D. & MUELLER, W. C. 2000 Scaling properties of three-dimensional isotropic magnetohydrodynamic turbulence. *Phys. Plasmas* **7**, 4889–4899.
- BRANDENBURG, A. 2001 The inverse cascade and non-linear alpha-effect in simulations of isotropic helical turbulence. *Astrophys. J.* **550**, 52117, 1–17.
- BUSSE, F. H. 1971 Bewegungen im Kern der Erde. *Z. Geophysik* **37**, 153–177.
- BUSSE, F. H. 1978 Magnetohydrodynamics of the Earth's dynamo. *Annu. Rev. Fluid Mech.* **10**, 435–462.
- BUSSE, F. H. 1992 Dynamo theory of planetary magnetism and laboratory experiments. In *Evolution of Dynamical Structures in Complex Systems* (ed. R. Friedrich & A. Wunderlin), pp. 359–384. Springer.
- BUSSE, F. H. 1994 Convection driven zonal flows and vortices in the major planets. *Chaos* **4**, 123–134.
- BUSSE, F. H. 2000 Homogeneous dynamos in planetary cores and in the laboratory. *Annu. Rev. Fluid Mech.* **32**, 838–308.
- BUSSE, F. H. & CARRIGAN, C. R. 1974 Convection induced by centrifugal buoyancy. *J. Fluid Mech.* **62**, 579–592.
- BUSSE, F. H. & CARRIGAN, C. R. 1976 Laboratory simulation of thermal convection in rotating planets and stars. *Science* **191**, 81–93.
- CARRIGAN, C. R. & BUSSE, F. H. 1983 An experimental and theoretical investigation of the onset of convection in rotating spherical shells. *J. Fluid Mech.* **126**, 287–305.

- CHILDRESS, S. 1967 A class of solutions of the magnetohydrodynamic dynamo problem. In *The Application of Modern Physics to the Earth and Planetary Interiors, Proc. NATO Adv. Study Inst. Newcastle* (ed. S. K. Rundcorn). Wiley-Interscience.
- DAVIDSON, P. A. 2001 *An Introduction to Magnetohydrodynamics*. Cambridge University Press.
- FEARN, D. R. 1998 Hydromagnetic flow in planetary cores. *Rep. Prog. Phys.* **61**, 175–235.
- FRISCH, U., POUQUET, A., LEORAT, J. & MAZURE, A. 1975 Possibility of an inverse cascade of magnetic helicity in magnetohydrodynamic turbulence. *J. Fluid Mech.* **68**, 769–778.
- GAILITIS, A. 1967 Self-excitation conditions for a laboratory model of a geomagnetic dynamo. *Magnetohydrodynamics* **3**, 23–29.
- GAILITIS, A., LIELAUSIS, O., DEMENTEV, S., PLATACIS, E., CIFERSONS, A., GERBETH, G., GUNDRUM, TH., STEFANI, F., CRISTEN, M., HAENEL, H. & WILL, G. 2001 Magnetic field saturation in the Riga dynamo experiment. *Phys. Rev. Lett.* **86**, 3024–3027.
- GAILITIS, A., LIELAUSIS, O., PLATACIS, E., GERBETH, G. & STEFANI, F. 2002 Laboratory experiments on hydromagnetic dynamos. *Rev. Mod. Phys.* **74**, 973–990.
- GLATZMAIER, G. A. 2002 Geodynamo simulations – how realistic are they? *Annu. Rev. Earth Planet. Sci.* **30**, 237–257.
- GLATZMAIER, G. A. & ROBERTS, P. H. 2000 Geodynamo theory and simulations. *Rev. Mod. Phys.* **72**, 1081–1123.
- GOLUBITZKY, M. & SCHAEFFER, G. D. 1985 *Singularities and Groups in Bifurcation Theory*. Springer.
- GRAPPIN, R., POUQUET, A. & LEORAT, J. 1983 Dependence of MHD-turbulence spectra on the velocity-magnetic field correlation. *Astron. Astrophys.* **126**, 51–58.
- HINZE, J. O. 1975 *Turbulence*. McGraw-Hill.
- IROSHNIKOV, P. S. 1963 Turbulence of a conducting fluid in a strong magnetic field. *Sov. Astron.* **7**, 566–571.
- JONES, C. A. 2000 Convection-driven geodynamo models. *Phil. Trans. R. Soc. Lond. A* **358**, 873–897.
- JOOS, G. & JOSEPH, D. D. 1980 *Elementary Stability and Bifurcation Theory*. Springer.
- KOLESNIKOV, Y. B. & TSINOBER, A. B. 1974 Experimental investigation of two dimensional turbulence behind a grid. *Magnetohydrodynamics* **10**, 621–624.
- KOLMOGOROV, A. N. 1941 Local structure of turbulence in an incompressible fluid at large Reynolds numbers. *Dokl. Akad. Nauk. SSSR* **30**, 299–303.
- KRAICHNAN, R. H. 1965 Inertial range spectrum in hydromagnetic turbulence. *Phys. Fluids* **8**, 1385–1387.
- LEORAT, J., POUQUET, A. & FRISCH, U. 1981 Fully developed MHD-turbulence near critical magnetic Reynolds numbers. *J. Fluid Mech.* **104**, 419–443.
- MARIE, L., BURGUETE, J., CHIFFAUDEL, A., DAVIAUD, F., ERICHER, D., GASQUET, C., PETRELIS, F., FAUVE, S., BOURGOIN, M., MOULIN, M., ODIER, P., PINTON, J. F., GUIGON, A., LUCIANI, J. B., NAMBER, F. & LEORAT, J. 2001 MHD in von Karman swirling flows. In *Dynamo and Dynamics, a Mathematical Challenge* (ed. D. Armbruster & J. Opera). Nato Science Series, vol. 26.
- MESSADEK, K. & MOREAU, R. 2002 An experimental investigation of MHD quasi-two-dimensional turbulent shear flows. *J. Fluid Mech.* **456**, 37–159.
- MOFFATT, H. K. 1961 The amplification of a weak applied magnetic field by turbulence in fluids of moderate conductivity. *J. Fluid Mech.* **11**, 625–635.
- MOSS, D. 1997 Dynamo generation of cosmic magnetic fields. *Contemp. Phys.* **18**, 49–62.
- MUELLER, U., STIEGLITZ, R. & HORANYI, S. 2002 The Karlsruhe Dynamo Experiment. *Tech. Rep. Forschungszentrum Karlsruhe, FZKA 6756*.
- ODIER, P., PINTON, J. F. & FAUVE, S. 1998 Advection of a magnetic field by a turbulent swirling flow. *Phys. Rev. E* **58**, 7397–7401.
- PEFFLEY, N. L., CAWTHORNE, A. B. & LATHROP, D. P. 2000 Toward a self-generating dynamo: The role of turbulence. *Phys. Rev. E* **61**, 5287–5296.
- POUQUET, J., FRISCH, U. & LEORAT, J. 1976 Strong MHD helical turbulence and the non-linear dynamo effect. *J. Fluid Mech.* **77**, 321–354.
- RÄDLER, K.-H. 1995 Cosmic dynamos. *Rev. Mod. Astron.* **8**, 295–321.
- RÄDLER, K.-H., APSTEIN, E., RHEINHARDT, M. & SCHUELER, M. 1998 The Karlsruhe dynamo experiment, a mean field approach. *Studia geophys. et geod.* **42**, 320–327.
- RÄDLER, K.-H., RHEINHARDT, M., APSTEIN, E. & FUCHS, H. 2002a On the mean-field theory of the Karlsruhe dynamo experiment. 1. Kinematic theory. *Magnetohydrodynamics* **38**, 41–71.



- RÄDLER, K.-H., RHEINHARDT, M., APSTEIN, E. & FUCHS, H. 2002*b* On the mean-field theory of the Karlsruhe dynamo experiment. 2. Back-reaction of the magnetic field on the fluid flow. *Magnetohydrodynamics* **38**, 73–94.
- RITTINGHOUSE INGLIS, D. 1981 Dynamo theory of the Earth's varying magnetic field. *Rev. Mod. Phys.* **53**, 481–496.
- ROBERTS, G.-O. 1970 Spatially periodic dynamos. *Phil. Trans. R. Soc. Lond. A* **266**, 535–558.
- ROBERTS, G.-O. 1972 Dynamo action of fluid motions with two-dimensional periodicity. *Phil. Trans. R. Soc. Lond. A* **271**, 411–453.
- STEENBECK, M., KRAUSE, F. & RÄDLER, K.-H. 1966 Berechnungen der mittleren Lorentz Feldstärke für ein elektrisch leitendes Medium in turbulenter, durch Corioliskräfte beeinflusste Bewegung. *Z. Naturforschung* **21**, 368–376.
- STIEGLITZ, R. & MÜLLER, U. 1996 GEODYNAMO: Eine Versuchsanlage zum Nachweis des homogenen Dynamoeffekts; *Wissenschaftlicher Bericht FZKA* 5716.
- STIEGLITZ, R. & MÜLLER, U. 2001 Experimental demonstration of the homogeneous two-scale dynamo. *Phys. Fluids* **13**, 561–564.
- SUMITA, I. & OLSON, P. 2000 Laboratory experiments on high Rayleigh number thermal convection in a rapidly rotating hemispherical shell. *Phys. Earth Planet. Inter.* **117**, 153–170.
- TILGNER, A. 1997 A kinematic dynamo with a small scale velocity field. *Phys. Lett. A* **226**, 75–79.
- TILGNER, A. 2002 Numerical simulation of the onset of dynamo action in an experimental two-scale dynamo. *Phys. Fluids* **14**, 4092–4094.
- TILGNER, A. & BUSSE, F. H. 2002 Simulation of the bifurcation diagram of the Karlsruhe dynamo. *Magnetohydrodynamics* **38**, 35–40.
- ZHANG, K. 1992 Spiralling columnar convection in rapidly rotating spherical shells. *J. Fluid Mech.* **236**, 535–556.